Jet-induced mixing mechanisms in a novel pond geometry

Imane Skifa, Andrés Cimino, Pierre-Henri Cocquet, Nicolas Chauchat, Yves Le Guer

Jet-Induced Mixing Mechanisms in a Novel Pond Geometry

Imane Skifa*[1], Andrés Cimino[1], Pierre-Henri Cocquet[1], Nicolas Chauchat[1], Yves le Guer[1]

[1]Laboratoire des Sciences de l'Ingénieur Appliquées à la Mécanique et au Génie Electrique (SIAME), Fédération IPRA-CNRS, Université de Pau et des Pays de l'Adour E2S UPPA, 64000, Pau, France

*Corresponding author at: Laboratoire SIAME, Bâtiment IPRA, Avenue de l'Université, 64000 Pau France. Email address: imane.skifa@univ-pau.fr

Abstract

This study examines the mixing performance of a novel raceway pond design actuated by lateral oscillating jets, using Computational Fluid Dynamics (CFD) simulations with passive scalar transport modeling as a theoretical framework for quantifying homogenization. Two jet operation strategies are investigated: a fixed single-configuration mode (Case 1) and a time-alternating configuration mode (Case 2). Mixing efficiency is evaluated through time-resolved concentration fields and quantified using complementary indicators, namely the scalar variance, the L^2 norm of concentration gradients, and the mix-norm. The results show that alternating jet actuation (Case 2) significantly enhances homogenization. Specifically, the scalar variance decays 41% faster and the mix-norm decreases over twice as rapidly compared to Case 1. The gradient norm exhibits a pronounced rise followed by rapid decay once jet switching is initiated at 20 s, indicating accelerated filament stretching and breakup of unmixed regions. As a result, Case 2 reaches a near-uniform concentration state approximately 30% earlier than Case 1. The improved performance is attributed to the periodic disruption of coherent vortical structures, which intensifies Lagrangian stretching and folding and thereby accelerates diffusion-driven mixing. These findings highlight the potential of time-modulated jet operation to improve operational efficiency in microalgal raceway ponds while offering a mechanically flexible alternative to conventional mixing technologies.

Keywords— Microalgae, Cultivation pond , CFD simulations, Mixing Strategy, Oscillating jets

1 Introduction

The growing global population and industrialization have intensified the demand for sustainable energy, food, and feed solutions. In response, the bio-economy has emerged as a key strategy to align human development with ecological preservation. Biomass energy is central to this effort, offering renewable fuels and helping reduce atmospheric CO_2. However, large-scale bioenergy production often requires significant land and water resources, raising environmental concerns.

Microalgae have gained attention as one of the most promising sources of photosynthetic biomass (Rogers et al., 2014). They efficiently convert sunlight and CO_2 into valuable biochemicals—such as lipids, proteins, carbohydrates, and pigments—and can be cultivated without using arable land or competing with food crops (Oncel, 2013; Satyanarayana et al., 2011; Shuba and Kifle, 2018; Singla et al., 2010). Their ability to thrive in extreme conditions, including saline water and wastewater (Narala et al., 2016; Oncel, 2013), along with their high growth rates, make them ideal candidates for sustainable biofuel production.

The development of large-scale microalgae cultivation has progressed from early controlled systems to more scalable and cost-effective open methods. While closed photobioreactors offer control over contamination and environmental parameters, open-air systems—such as ponds, tanks, and especially raceway ponds—enable greater scalability using natural sunlight and atmospheric CO_2. Raceway ponds, in particular, have become the most widely used open system due to their simple design, low operational costs, and effective mixing, which enhances light exposure and nutrient distribution. First introduced in large-scale cultivation by Johnson et al. (1988), raceway ponds remain a standard in microalgae production and have been extensively studied and optimized (Andersen, 2005; Skifa et al., 2024).

Achieving optimal mixing in raceway ponds requires more than mechanical design; it demands an understanding of the underlying fluid dynamics. The study of mixing predates formal publications, yet the notion of a "well-mixed" system is often treated as self-evident (Kukukova et al., 2009). Despite this perception, mixing is a dynamic, multiscale process essential for achieving uniformity in systems such as raceway ponds, and its complexity is widely recognized across disciplines (Aref et al., 2017).

Modeling these processes is challenging because fluid dynamics itself is complex, particularly when dealing with non-Newtonian fluids whose properties depend on local composition and shear rate (Castillo-Sánchez et al., 2022; De Roma et al., 2024). Many such fluids also exhibit viscoelasticity, yield stress, or shear-thinning behavior, especially at small length scales and in non-uniform mixtures (De Roma et al., 2024). Capturing all these effects simultaneously is difficult, as simulation accuracy relies heavily on reliable rheological data, geometric details, and boundary conditions (De Roma et al., 2024). Consequently, mixing studies have often been approached case-by-case. Recent advances, however, combining experiments with kinematics, dynamical systems, and chaos theory, now offer a more unified framework (Aref et al., 2017; Kelley and Ouellette, 2011).

Terminology in the literature is not always consistent, and "mixing" and "stirring" are frequently used interchangeably (Villermaux, 2019). Here, we distinguish the two: stirring refers to the advective deformation of fluid elements—stretching and folding—that increases interfacial area (Gepner and Floryan, 2020; Kelley and Ouellette, 2011). Mixing combines stirring with molecular diffusion, ultimately leading to a uniform composition (Villermaux, 2019). Stirring generates fine structures on which diffusion can act efficiently (Kelley and Ouellette, 2011), and these interactions become particularly intricate in chaotic flows, where underlying dynamical structures can be measured.

A widely used definition describes mixing as the process that drives a system from an initially heterogeneous state to a uniform one (Villermaux, 2019). This homogenization occurs through the spreading of a scalar tracer and the continuous deformation of fluid elements by velocity gradients and shear, leading to a progressive loss of spatial structure (Karrasch and Keller, 2020). Although molecular diffusion can continue to act at very small scales, mixing is fundamentally an irreversible process in which initial conditions are

lost.

However, mixing is not always strictly irreversible. When stretching is weak and diffusion is the dominant mechanism, scalar evolution may appear quasi-reversible, as reversible advective effects can be separated from the irreversible joint action of advection and diffusion (De Roma et al., 2024). In such cases, concentration structures may persist or even re-emerge under flow reversal in low-Reynolds-number creeping flows, where diffusion alone is insufficient for complete homogenization (Gepner and Floryan, 2020). This behavior underscores the essential role of sustained stretching and folding in producing truly irreversible mixing.

Mixing is a central process in fluid dynamics, critical to the transport of mass, energy, and momentum across a wide range of natural and engineered systems. The classical distinction between turbulent and laminar mixing has long guided our understanding of scalar transport, yet modern perspectives—particularly those rooted in nonlinear dynamics—have significantly expanded this framework. One of the most influential advances in the theoretical study of mixing is the concept of chaotic advection, introduced by Aref (1987), which reveals that complex, space-filling particle trajectories can arise even in laminar, deterministic flows. This phenomenon occurs through repeated stretching and folding of material lines, leading to exponential separation of nearby fluid parcels and enhanced scalar homogenization. The realization that chaos can emerge in simple, steady or periodically forced flows transformed the field, offering a new lens through which to interpret mixing without relying on turbulence. Ottino (1989) formalized this understanding by integrating tools from dynamical systems theory to describe how topological complexity, flow symmetries, and time-dependence govern mixing quality. His work emphasized that efficient mixing is less about flow intensity and more about how the flow moves and deforms material volumes. Key mechanisms such as streamline crossing, transient islands, and hyperbolic points contribute significantly to the creation of fine-scale striations that diffusion can then act upon. Further development of the field has led to the identification of Lagrangian Coherent Structures (LCS), which act as the "skeletons" of fluid motion, organizing patterns of transport and revealing barriers or corridors of mixing (Haller, 2015a). These structures generalize the notion of stable and unstable manifolds in time-dependent flows and provide a quantitative framework for diagnosing transport behavior. In parallel, the use of finite-time Lyapunov exponents (FTLE) has become a standard approach for visualizing and quantifying stretching fields, making the Lagrangian description more computationally accessible.

Aref et al. (2017), in their comprehensive review Frontiers of Chaotic Advection, synthesized decades of progress, highlighting key themes such as the role of geometry, boundary conditions, and flow periodicity in driving mixing. They also underscored the universality of chaotic mixing mechanisms across scales—from microfluidic devices to geophysical flows—emphasizing that the underlying mathematics is often independent of the physical medium. Their work outlines how advances in theory, experimentation, and computation have converged to form a unified picture of mixing that is both predictive and design-oriented. Another vital contribution comes from the study of topological chaos, where braid theory and topological entropy are used to quantify the minimal complexity required for effective mixing (Thiffeault, 2005, 2022). This approach connects mixing efficiency to the braiding of material lines by moving stirrers or time-dependent flows, providing rigorous lower bounds on the amount of stretching achievable in a system. Importantly, mixing is not only a kinematic phenomenon—it also intersects with thermodynamics, reaction kinetics, and mass transfer. The interaction between fluid deformation and scalar diffusion ultimately determines the rate at which concentration gradients decay, and understanding this interaction is crucial for applications ranging from chemical engineering to biological transport. Theoretical frameworks such as Batchelor's regime describe the scalar cascade in high-Péclet-number flows, bridging molecular diffusion with advective stirring at intermediate scales (Batchelor, 1959).

Despite considerable progress in reactor design, achieving efficient mixing in raceway ponds (RWPs) remains a critical bottleneck, especially at industrial cultivation scales. Effective mixing must guarantee homogeneous distribution of light, nutrients, and dissolved gases, while also preventing sedimentation of cells and

thermal stratification—factors that directly determine biomass productivity and overall process efficiency. Yet, mixing in RWPs is inherently difficult: their shallow depth, large surface-to-volume ratio, and open-channel hydrodynamics produce strongly anisotropic flows that foster dead zones and weak circulation near the bottom, limiting both mass and momentum transfer.

Traditionally, RWPs employ paddlewheels to drive bulk circulation of the culture medium, generating large-scale unidirectional flow loops. While effective at sustaining overall motion, this approach provides limited local stirring, particularly near channel walls, corners, and other poorly flushed regions where insufficient vertical mixing strongly reduces the applicability of raceway ponds (Akca et al., 2024; Shen and Dandy, 2024). Compared with turbulent flow conditions, paddlewheel-driven flows produce larger dead zone volumes with reduced turbulence intensity (Ali et al., 2015). As a result, homogenization of scalar fields such as nutrients or dissolved CO_2 remains incomplete, leading to strong spatial heterogeneity in microalgae light exposure and growth conditions as evidenced by CFD studies of real-scale raceway reactors (Ali et al., 2015).

Vertical mixing is particularly problematic in paddlewheel-driven systems. Studies have shown that paddlewheels create relatively weak swirling motions that do not persist for long distances downstream (Shen, 2021), with typical flow velocities maintained between 0.10–0.20 m/s to prevent sedimentation while avoiding excessive shear stress (Rajput et al., 2025). This weak turbulence generation fosters boundary layer development along the bed and walls, while at the free surface the reduced mixing intensity promotes fluid thinning and stratification, further restricting vertical transport.

Although increasing paddlewheel RPM could theoretically enhance turbulence, this approach faces critical practical limitations. Paddlewheel power consumption increases significantly with rotational speed, with typical values ranging from 30 $W.m^{-3}$ at optimal operating conditions (Li et al., 2014), making high-speed operation economically unfeasible for industrial-scale facilities covering hectares of surface area as documented in energy balance analyses of raceway pond systems (Li et al., 2014). Moreover, excessive paddlewheel speeds create heavy shear stress that can damage shear-sensitive microalgae strains (Eltanahy et al., 2018) as high velocities and intensive mixing have been shown to inhibit biomass growth.

Compounding these drawbacks, paddlewheel-driven flows typically produce pulsating velocity profiles with reduced shear stress and turbulence compared to continuous turbulent conditions (Ali et al., 2015) that inhibit the formation of fine-scale vortical structures—structures that are crucial for enhancing diffusion and local mixing.

In raceway ponds, turbulent mixing is often avoided due to its high energy requirements and potential shear-induced damage to sensitive microalgae cells. This limitation raises a fundamental question: *how can we harness chaotic advection mechanisms in the design of raceway ponds to enhance mixing performance without relying on turbulent flow regimes or energy-intensive operation?* Chaotic advection, as demonstrated in theoretical and laboratory-scale studies, offers a promising approach by leveraging stretching and folding of fluid elements even in laminar settings (Thiffeault, 2012). However, implementing such mechanisms in large-scale ponds requires new design principles that move beyond continuous flow loops.

In this study, we investigate a novel "unit mixing" strategy in which mixing is driven not by global recirculation, but through localized, alternating lateral jets that periodically inject fluid from the sides of a rectangular raceway pond. These pump-driven inlets, positioned on opposite walls, are designed to emulate oscillating jet flows known for generating complex, time-dependent vortical structures. By breaking the symmetry of steady-state flows, this configuration induces chaotic-like advection, promoting enhanced scalar dispersion and more effective reduction of concentration gradients than traditional paddlewheel systems (Skifa et al., 2024). To analyze the hydrodynamic and mixing behavior of this geometry, we perform a two-dimensional CFD study as an initial investigation. While vertical transport mechanisms require future 3D modeling for full characterization, the shallow geometry of raceway ponds—where depth-to-length ratios are typically below 1:20—justifies a 2D approach to capture dominant horizontal advection-diffusion

processes. This allows for computational efficiency while still yielding key insights into lateral mixing dynamics.

To evaluate the performance of the proposed jet-based configuration, we conduct CFD simulations that track both the fluid flow and the transport of a passive scalar. Mixing is quantified using a suite of scalar indicators—including concentration variance, spatial gradients, and mix-norm evolution—that capture both the magnitude and spatial scale of scalar heterogeneity. We do not employ LCS or FTLE diagnostics, as our focus is on Eulerian metrics that directly quantify scalar homogenization and enable systematic classification of jet protocols, whereas Lagrangian tools, though insightful, are computationally heavier and less aligned with the comparative framework of this work. The objectives of this study are threefold: (i) to introduce a novel raceway pond mixing mechanism based on chaotic advection, leveraging alternating lateral jets instead of conventional paddlewheels; (ii) to systematically assess mixing performance using multiple scalar indicators that reveal different aspects of homogenization; and (iii) to establish a methodological framework for optimizing mixing strategies in photobioreactor design, providing theoretical insight and practical guidance for microalgae cultivation systems.

The principal innovation of this study lies in the introduction and assessment of a novel raceway pond mixing device that employs lateral oscillating jets as an alternative to conventional paddlewheels. To our knowledge, such a configuration has not been previously reported in the literature. This design seeks to exploit mechanisms of chaotic advection—periodic stretching and folding of fluid elements—to enhance homogenization under laminar operating conditions typical of microalgae raceways. Unlike steady circulation systems that produce quasi-stationary flow loops, the alternating jet actuation periodically disrupts coherent flow structures, fostering rapid dispersion of scalar concentrations and improved nutrient and light distribution. This approach provides a new pathway for improving hydrodynamic efficiency and mixing performance in large-scale open photobioreactors, while maintaining simplicity and low energy cost. The present study adopts a staged approach, positioning these numerical results as a foundation to guide the design and implementation of forthcoming experimental validations and 3D simulations.

2 Materials & Methods

2.1 Geometry

The system is a horizontally oriented array of rectangular ponds with central symmetry designed to enhance mixing and mass transport for microalgae cultivation. Each pond has dimensions of horizontal width $B = 456$ mm and lateral height $H = 302$ mm. In the case of a conventional raceway pond, these would correspond to the streamwise (B) and spanwise (H) directions. However, in our design, there is no defined streamwise direction due to the central symmetry and bidirectional pumping, which results in a more isotropic horizontal flow field. The pond features two pairs of staggered nozzles that serve as inlets and outlets. These nozzles are connected via pipes and valves, allowing for flexible control of flow configurations. Fluid circulation within the system is driven by reversible axial flow pumps, which enable bidirectional flow and adaptability to various experimental conditions.

A two-dimensional (2D) geometry model is employed (Figure 1), representing a simplified version of the inherently three-dimensional (3D) system. In the physical setup, pipes with circular cross-sections run beneath the pond, whereas in the 2D model, the pipes are represented laterally to maintain visual clarity while preserving key hydrodynamic features.

Diffuser-type nozzle system is integrated into the design to prevent the formation of oscillatory jet instabilities that may arise when using straight, non-diffuser nozzles. Unlike conventional raceway pond (RWP) mixing mechanisms that rely on paddlewheels, this system employs a controlled jet-induced mixing strategy, offering several advantages. The modular units can be arranged in sequence. The design also allows for integration into existing RWP systems, improving mixing efficiency.

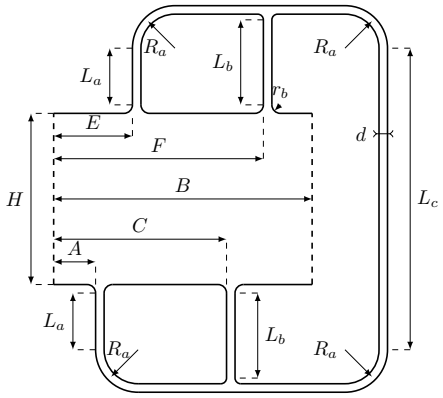

Figure 1: Top view of the 2D geometry of the pond and the piping system. pond has dimensions of horizontal width $B = 456$ mm and lateral height $H = 302$ mm. The geometry exhibits central symmetry about the vertical axis, implying that the inlet–outlet pairs A and C, as well as E and F, occupy symmetric positions and yield equivalent flow characteristics when the direction is reversed. The bottom nozzles are located at coordinates $A = 50\,\text{mm}$ and $C = 281\,\text{mm}$, while the top nozzles are positioned at $E = 115\,\text{mm}$ and $F = 346\,\text{mm}$. All pipes have a diameter of $d = 12\,\text{mm}$. The system includes a minimal offset length $L_a = 100\,\text{mm}$ and a bend radius $R_a = 5d$ to minimize head losses and prevent flow instabilities. Additional dimensions include $L_b = 150\,\text{mm}$, $L_c = 628\,\text{mm}$, and $r_b = 10\,\text{mm}$

The nozzle shape follows an elliptical expansion profile, designed to gradually decelerate the flow during outflow and accelerate it during inflow, thereby reducing local head losses caused by abrupt cross-sectional changes. The transition from the inlet diameter to the outlet diameter follows a fixed geometric law—specifically, the nozzle ellipse law—which creates a smooth and continuous variation in flow area. Although the geometry is fixed, this design directly influences the velocity gradient $\nabla\vec{u}$ by shaping the axial acceleration (or deceleration) along the nozzle length. The gradual expansion creates a spatially distributed shear field that inhibits the development of Kelvin–Helmholtz instabilities, thereby contributing to overall flow stability. The ratio of diameters is $D_{\text{inlet}}/D_{\text{outlet}} = 12/60 = 1/5$. This progressive expansion helps mitigate excessive recirculation that could cause flow inefficiencies, while still allowing flow instabilities and separation phenomena to develop in a controlled manner. It should also be noted that the nozzle design is fully reversible, allowing both inflow and outflow operations without loss of geometric symmetry, which is essential for bidirectional pumping and alternating flow protocols.

2.2 Numerical Model

The full fluid flow and scalar transport problem is governed by the time-dependent incompressible Navier–Stokes equations coupled with the scalar transport equation, which describe the evolution of velocity and concentration fields as functions of time and space. In this study, the scalar is considered passive, meaning it is advected and diffused by the flow but does not influence the fluid dynamics.

$$\nabla \cdot \vec{u} = 0, \tag{1}$$

$$\rho\frac{\partial \vec{u}}{\partial t} + \rho(\vec{u}\cdot\nabla)\vec{u} = -\nabla p + \mu\nabla^2\vec{u} + \vec{S}_{\text{momentum}}, \tag{2}$$

$$\frac{\partial \varphi}{\partial t} + \vec{u}\cdot\nabla\varphi = k\nabla^2\varphi. \tag{3}$$

Here, $\vec{u}$ is the velocity vector, p is the pressure, φ is the scalar concentration, and $\vec{S}_{\text{momentum}}$ represents momentum source terms such as those from jet actuation.

To better interpret the influence of flow and transport parameters, the equations are expressed in nondimensional form using the characteristic length L, velocity U, time scale $T = L/U$, pressure scale $P = \rho U^2$ (with ρ the fluid density), and scalar scale Φ. The dimensionless variables are defined as:

$$\mathbf{x}^* = \frac{\mathbf{x}}{L}, \quad t^* = \frac{tU}{L}, \quad \vec{u}^* = \frac{\vec{u}}{U}, \quad p^* = \frac{p}{\rho U^2}, \quad \varphi^* = \frac{\varphi}{\Phi}. \tag{4}$$

Substituting these variables into Eqs. (1)–(3) and omitting the asterisks for clarity yields the nondimensional system:

$$\nabla \cdot \vec{u} = 0, \tag{5}$$

$$\frac{\partial \vec{u}}{\partial t} + (\vec{u}\cdot\nabla)\vec{u} = -\nabla p + \frac{1}{\mathrm{Re}}\nabla^2\vec{u} + \vec{S}^*, \tag{6}$$

$$\frac{\partial \varphi}{\partial t} + \vec{u}\cdot\nabla\varphi = \frac{1}{\mathrm{Pe}}\nabla^2\varphi. \tag{7}$$

Here, $\mathrm{Re} = \dfrac{\rho UL}{\mu}$ is the Reynolds number, where μ is the dynamic viscosity of the fluid, and $\mathrm{Pe} = \dfrac{UL}{k}$ is the Péclet number, where k is the molecular diffusivity of the scalar. The Péclet number can also be expressed as $\mathrm{Pe} = \mathrm{Re}\,\mathrm{Sc}$ using the Schmidt number $\mathrm{Sc} = \mu/(\rho k)$. The nondimensional source term $\vec{S}^* = \vec{S}_{\text{momentum}}L/(\rho U^2)$ quantifies the relative forcing intensity.

These nondimensional parameters govern the relative importance of inertia, viscous diffusion, and scalar transport. In this work, low Reynolds numbers confirm laminar flow conditions, while high Péclet numbers indicate advection-dominated scalar transport—favorable for studying chaotic mixing under laminar regimes that preserve microalgal integrity.

The governing equations are solved numerically within the finite-volume framework using a collocated arrangement for all variables, including velocity $\vec{u}$, pressure p, and the passive scalar φ. Spatial discretization is performed with second-order accurate schemes for all variables to reduce numerical diffusion. Specifically, the advection terms in the momentum and scalar transport equations are discretized using the Second-Order Upwind scheme, while pressure is interpolated with a second-order scheme. Gradients, $\nabla\phi$, are reconstructed using the Green–Gauss cell-based method, and the Laplacian operator, $\Delta\phi$, is discretized consistently with the finite-volume approach using face-based fluxes. To prevent pressure–velocity decoupling, Rhie–Chow interpolation is applied.

Temporal derivatives are approximated using an implicit first-order scheme. For pseudo-transient steady-state simulations, a fixed time step of $dt = 0.1$ s is used, allowing the solution to march iteratively toward convergence over long physical times without representing real unsteadiness. For fully transient simulations, an adaptive implicit time-stepping strategy is employed to enhance stability during complex pumping cycles or sudden flow changes.

The computational domain consists of a closed two-dimensional region divided into two fluid zones: the pond, representing the main reservoir, and a piping system connecting the nozzles to enable controlled recirculation (Figure 1). The flow is assumed incompressible, and the Coupled scheme is used for pressure–velocity coupling to ensure stability in convection-dominated regimes. Convergence is monitored through residuals, defined as the normalized imbalance of each transport equation:

$$R_\phi = \frac{\sum_i |\text{source}_i - \text{flux}_i|}{\sum_i |\text{source}_i|},$$

where the sum runs over all control volumes and ϕ represents any transported variable (u, v, p, or φ). The solution is considered converged when all residuals fall below 10^{-6} and the tracer mass imbalance, defined as the relative change of total tracer mass between iterations, is below 0.1%. The concentration field is modeled as a passive scalar, enabling nearly convection-dominated transport. To sustain the desired laminar flow profile within the closed piping network—where no physical inlets or outlets are prescribed—volumetric momentum source terms $\vec{S}_{\text{momentum}}$ are applied in localized regions. We emphasize that laminar flow is deliberately chosen to exploit chaotic advection rather than turbulent mixing: time-periodic protocols create efficient mixing through deterministic stretching and folding (Aref, 1987; Ottino, 1989) while avoiding shear damage to microalgae cells (Skifa et al., 2024). Here, "laminar flow profile" refers specifically to the velocity distribution within the pipes (necessary for momentum source implementation), not to the quality of mixing achieved in the pond. These internal body forces replace traditional inflow/outflow boundary conditions and are designed to drive the flow self-consistently within the domain. Depending on the pumping configuration, source terms are applied either in the x-direction ($pump_0$ or $pump_2$) or the y-direction ($pump_1$).

The magnitude of $\vec{S}_{\text{momentum}}$ is estimated using one-dimensional control volume analysis based on energy conservation, as illustrated in Figure 2b. The control volume is constructed according to the jet pathway, and the pressure gradient needed to sustain the target mean velocity is calculated using analytical head loss models such as Darcy's law, corrected by the empirical friction factor f_B (Fox et al., 2020). The resulting pressure gradient is then translated into an equivalent body force and implemented numerically as a source term.

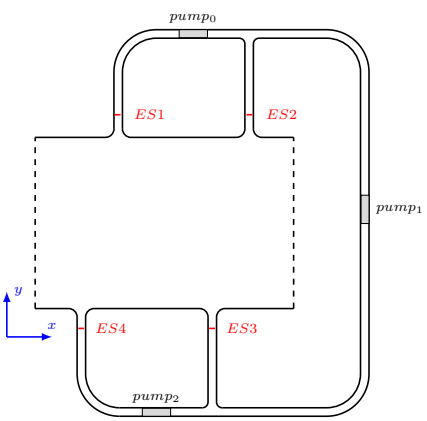

(a) Fluid zones in the computational domain and fluid interfaces at the nozzles. The domain includes four openings (ES1, ES2, ES3, ES4) connected via three pumps ($pump_0$, $pump_1$, $pump_2$) that drive the flow between the inlet–outlet pairs. Periodic boundary conditions are applied along the left and right lateral walls, allowing flow and scalar quantities to re-enter the domain from the opposite side and preserving continuity across the transverse direction

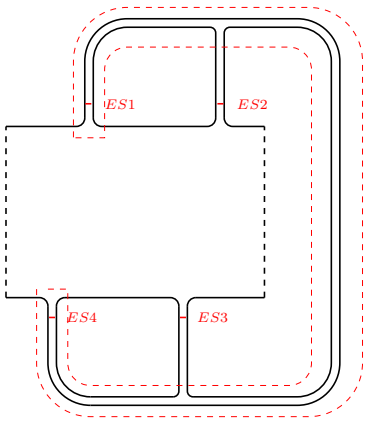

(b) Control volume to estimate the pressure jump for a flow from ES1 to ES4

Figure 2: Computational domain and control volume for estimating pressure jump in lateral jet configuration

$$\Delta p_{\text{pump}} = S_{\text{momentum}} \cdot L_s, \tag{8}$$

$$\frac{\Delta p_{\text{pump}}}{\rho} = f_D \frac{L_{\text{st}}}{D_h} \frac{U^2}{2} + f_B \frac{L_B}{D_h} \frac{U^2}{2}, \tag{9}$$

where L_s is the length over which the momentum source is applied, L_{st} is the total length of straight sections, and L_B is the effective length associated with bend-induced losses. The Darcy friction factor, originally derived for fully developed laminar flow in circular pipes, is expressed as $f_D = 64/Re$. An empirical bend correction $f_B = 0.698$ from Spedding et al. (2004), based on 3D pipe experiments, is applied to account for additional head losses at flow turns. Although both correlations originate from three-dimensional internal flows, they are here adapted to the present two-dimensional configuration by redefining the hydraulic diameter as $D_h = 2d$, corresponding to a planar channel of height d and effectively infinite width. In this 2D framework, the empirical constants are interpreted as analogues rather than direct physical matches to 3D flows, providing a first-order estimate of viscous and bend-induced losses.

The mass flow rate $\dot{m}$ is estimated via the Darcy–Weisbach equation:

$$\frac{\Delta p_{\text{pump}}}{L} = f_D \frac{\rho U^2}{2 D_h}, \tag{10}$$

from which the flow velocity U, volumetric flow rate $Q = A_c U$, and mass flow rate $\dot{m} = \rho Q$ are deduced, where A_c is the cross-sectional area of the flow channel.

Since $\vec{S}_{\text{momentum}}$ is applied component-wise in Eqs. (2), we define its components based on the pressure gradient:

$$S_x = \pm \frac{\Delta p_{\text{pump}}}{L_s}, \quad S_y = \pm \frac{\Delta p_{\text{pump}}}{L_s}, \tag{11}$$

where the sign is chosen based on the direction of flow imposed by the active pump (e.g., `pump0`, `pump1`, or `pump2`). These values are inserted into the conservative form of the momentum equations in the x and y directions through the source term vector $\vec{S}_{\text{momentum}} = (S_x, S_y)$ (Appendix A.2).

As the pond domain is closed, no mass enters or leaves through boundaries; therefore, no Dirichlet or Neumann conditions are applied to simulate inflow or outflow. On solid walls, classical no-slip and no-flux conditions are enforced:

$$\vec{u} = 0, \quad \frac{\partial \varphi}{\partial n} = 0.$$

Periodic boundary conditions are used on lateral boundaries to emulate geometric or flow symmetries. This setup ensures that flow generation is fully governed by the internal momentum source $\vec{S}_{\text{momentum}}$, without the need to define inlet or outlet pressures or velocities. Scalar transport and flow development thus remain physically consistent throughout the domain. Initial conditions are specified by defining a velocity and scalar concentration field, representing an initial state from which the flow evolves. The scalar transport equation is initialized with either a uniform concentration field, $\varphi(\mathbf{x}, t = 0) = \varphi_0$, or a spatially varying distribution, for example, $\varphi(\mathbf{x}, t = 0) = \varphi_0 \, f(\mathbf{x})$, where $f(\mathbf{x})$ defines the initial spatial pattern. This allows the model to capture the evolution of mixing and transport phenomena from a well-defined initial state. The choice of numerical schemes, including the Rhie–Chow interpolation and the Coupled pressure–velocity solver, is consistent with the boundary conditions imposed at walls and periodic interfaces, ensuring stable and physically accurate treatment of pressure–velocity coupling.

To ensure the reliability of the simulation, convergence is monitored via report definitions such as mass flow rate through internal cross-sections, volume integrals of flow indicators, and scalar concentration statistics (mean and variance) (Appendix A.3), the internal flow rate stabilizes around the target value with minimal fluctuations, validating the implementation of the internal forcing through $\vec{S}_{\text{momentum}}$.

The computational domain is discretized using a hybrid unstructured mesh composed of quadrilateral and triangular cells (Figure 3). Quadrilateral elements are primarily used in the main flow region to reduce numerical diffusion along dominant streamlines, while triangular cells are employed near the nozzles and curved boundaries to ensure mesh conformity in high-gradient zones.

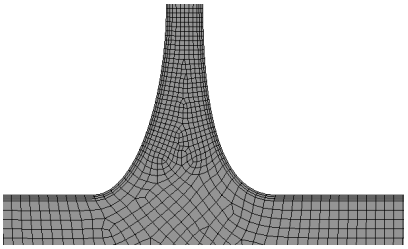

Figure 3: Hybrid mesh employed for the computational domain, with quadrilateral cells in the main flow region and triangular refinement near nozzle edges and walls.

Table I: Mesh statistics for the final discretization

Property	**Value**
Number of cells	45,601
Number of faces	93,588
Number of nodes	48,063
Characteristic element size	3.0×10^{-3} m
Cell volume range	2.56×10^{-7}–1.47×10^{-5} m^3
Face area range	2.72×10^{-4}–5.44×10^{-3} m^2
Mesh quality	No negative volumes, low skewness

Three meshes were evaluated to verify grid independence, corresponding to characteristic element sizes of 1×10^{-3} m (fine), 3×10^{-3} m (baseline), and 9×10^{-3} m (coarse), respectively. Mesh sensitivity was assessed using the temporal evolution of the scalar variance σ_φ^2, a key metric used throughout this study to quantify mixing performance. The coarse mesh exhibited an overly rapid decay of variance during the early stretching-dominated regime due to excessive numerical diffusion. In contrast, the baseline and refined meshes produced nearly identical results, with relative differences below 2

The choice of the baseline mesh can be further justified by a simple estimation: the pond cavity has an area of 0.302×0.456 m^2 $= 0.1377$ m^2, and with 45,601 cells, the average cell area is approximately 3×10^{-6} m^2, giving an average mesh length scale of $\sqrt{3 \times 10^{-6}} \approx 1.7$ mm. This indicates that scalar structures narrower than about 2 mm cannot be resolved, setting the effective resolution limit of the simulation. With a molecular diffusivity of $k \sim 10^{-9}$ m^2/s, any striation of 2 mm width would be smoothed out in roughly 1 h 7 min, consistent with the timescales observed in our simulations.

Given that further refinement would increase computational cost without significantly improving resolved scalar structures, the mesh based on an element size of 3×10^{-3} m was selected for all simulations.

Mesh quality was verified in ANSYS Fluent, confirming the absence of non-physical elements, smooth spatial transitions, and acceptable skewness levels for accurately resolving the strong advection and shear layers generated by the lateral jets. A periodic boundary condition is applied at the channel ends using a translation vector of $\Delta x = -0.456$ m to enable continuous recirculation. The main geometric and discretization characteristics of the final mesh are summarized in Table I.

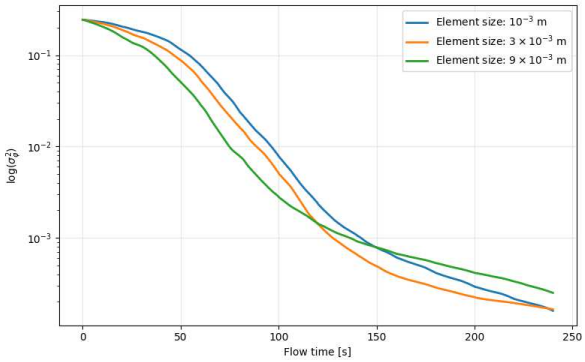

Figure 4: Mesh independence was evaluated by comparing the temporal evolution of the scalar variance σ_φ^2 on three different meshes, corresponding to characteristic element sizes of 9×10^{-3} m (coarse), 3×10^{-3} m (baseline), and 1×10^{-3} m (fine). All simulations were performed with a characteristic flow velocity of $U = 0.1$ m/s, fluid density $\rho = 1000$ kg/m^3, dynamic viscosity $\mu = 0.012$ Pa·s, scalar diffusivity $k = 10^{-9}$ m^2/s, and a fixed time step of $dt = 0.1$ s

2.3 Physical Model

The initial scalar distribution corresponds to a step-function initialization, where the pond domain (excluding the tubes) is divided into two distinct regions: one half initialized with a scalar concentration of 0, and the other half with a value of 1 (Figure 5). Such a binary initialization creates a sharp concentration gradient that allows for clear observation of diffusion and advection-driven mixing dynamics. Over time, as flow develops, the two regions begin to interpenetrate, and the scalar values smooth out.

To reflect real-world operating conditions, we selected a range of dynamic viscosities based on local farming practices and progressively increased them to evaluate mixing performance in more viscous media (more concentrated algal solutions to achieve the target of enhanced production rate). Local farmers typically handle suspensions with an effective viscosity approximately three to four times that of water, corresponding to algal biomass concentrations of around 1 to 2 g/L dry weight (DW), primarily due to the presence of algal biomass and eventually extracellular polymeric substances (EPS). Starting from this empirical baseline ($\mu \approx 3 \times 10^{-3}$ kg/(m.s)), we extend our study to cover a broader viscosity range (from $\mu = 0.004$ to 1.2 Pa.s) (Figure 6) aiming to ensure the system performs effectively even in highly viscous regimes. This approach anticipates scenarios of dense cultivation or advanced bioprocessing, where mixing remains a critical challenge. In addition, a fixed molecular diffusivity of $k = 1 \times 10^{-9}$ m^2/s was adopted to represent the transport of a passive scalar, such as a dissolved nutrient. This value is commonly used to approximate the diffusion of small molecules like fluorescein in water (Crank, 1979; Taylor, 1953). While actual diffusivities vary depending on the solute and the medium—ranging from 10^{-9} to 10^{-10} m^2/s for dissolved nutrients like nitrates and phosphates in algal suspensions, and significantly lower for diffusion across cellular membranes (on the order of 10^{-12} m^2/s), this value is therefore a first-order approximation with respect to solute-specific diffusivity variations, local microstructural effects, and other minor transport mechanisms, capturing primarily the macroscopic, advection-dominated behavior in the pond.

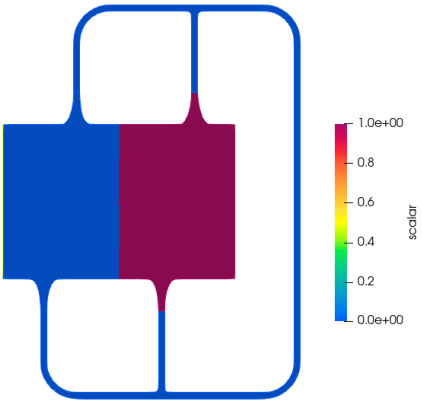

Figure 5: Initial scalar distribution in the domain. The domain was initialized with a sharp concentration gradient: one half of the pond was assigned a scalar value of 0, and the other half a value of 1. The dividing line between the two regions corresponds to the midline of the domain. Additionally, the lateral tubes were initialized with a scalar value of 0

We computed the local Reynolds and Péclet numbers for each selected viscosity (Table II), using a constant jet velocity $U = 0.1\,\mathrm{m/s}$, characteristic width $d = 0.012\,\mathrm{m}$ (corresponding to the nozzle or lateral jet diameter), and fluid density $\rho = 1000\,\mathrm{kg/m^3}$. This choice of characteristic length reflects the local flow features induced by the jets rather than the global domain dimensions (such as pond width B or depth H). Using the jet scale highlights the intensity of shear and inertial effects responsible for mixing in the injection zone. As shown, the Péclet number remains constant ($Pe \approx 1.2 \times 10^6$) for all test. This choice isolates

Table II: Reynolds number $Re = \rho U d/\mu$, Schmidt number $Sc = \mu/\rho k$, and Péclet number $Pe = Re \cdot Sc = Ud/k$ for different flow regimes with $U = 0.1\,\mathrm{m/s}$, $d = 0.012\,\mathrm{m}$ (Nozzle inlet), $\rho = 1000\,\mathrm{kg/m^3}$, and $k = 1 \times 10^{-9}\,\mathrm{m^2/s}$

Re	μ (Pa·s)	Sc	Pe
1	1.200	1.20×10^6	1.20×10^6
10	0.120	1.20×10^5	1.20×10^6
100	0.012	1.20×10^4	1.20×10^6
300	0.004	4.00×10^3	1.20×10^6

the effects of momentum diffusion (via μ) while keeping the scalar transport regime constant, allowing for a controlled investigation of how fluid viscosity affects flow patterns and mixing in the raceway pond. Within the piping system, designated regions are assigned momentum source terms, representing the action of pumps that drive the fluid through the tubes. Although the simulated velocity appears high relative to the small numerical domain, the design is dynamically scaled: matching Re and Pe ensures that the mixing mechanisms can be realistically translated to full-scale raceway ponds, where equivalent performance is

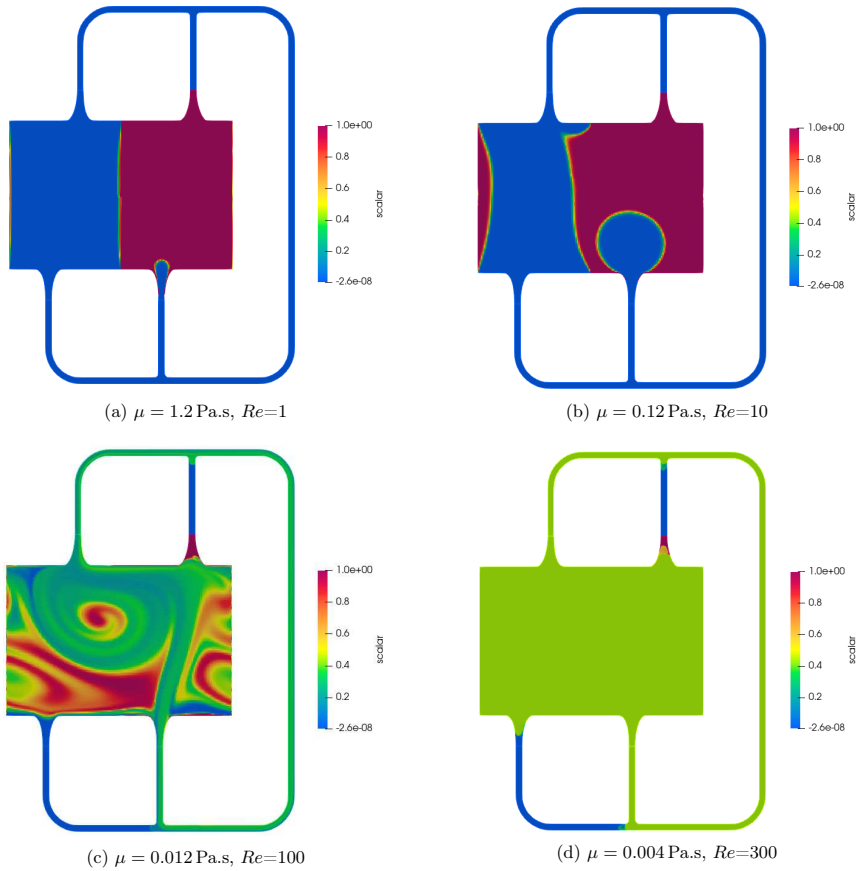

(a) $\mu = 1.2\,\text{Pa.s},\ Re$=1 (b) $\mu = 0.12\,\text{Pa.s},\ Re$=10

(c) $\mu = 0.012\,\text{Pa.s},\ Re$=100 (d) $\mu = 0.004\,\text{Pa.s},\ Re$=300

Figure 6: Evolution of scalar concentration distribution at t=60s for varying viscosity values in the ES3 $\rightarrow$ ES1 mixing configuration

achievable at lower absolute velocities and reduced pumping power.

Table III: Reynolds number comparison at different locations in the raceway pond system with $\mu = 0.012$ Pa·s and $\rho = 1000$ kg/m^3. Pond dimensions: $B = 0.456$ m (length), and $H = 0.302$ m (height)

Location	Characteristic Length	Velocity	Reynolds Number	Regime
Pipe (tube) / Nozzle inlet	$d = 0.012$ m	$U = 0.1$ m/s	$Re_{\text{pipe}} = 100$	Laminar
Nozzle outlet	$d_{\text{nozzle}} = 0.06$ m	$U_{\text{jet}} = 0.1$ m/s	$Re_{\text{nozzle}} = 500$	Laminar
Cavity (pond bulk)	$H = 0.302$ m	$U_{\text{cavity}} \approx 0.005$ m/s	$Re_{\text{cavity}} \approx 125$	Laminar

We computed the Reynolds number at three distinct scales to characterize the flow regime throughout the system (Table III). The computational domain measures $B = 0.456$ m in length and $H = 0.302$ m in height.

At the nozzle inlet (pipe), using the tube diameter $d = 0.012$ m and the imposed velocity $U = 0.1$ m/s, the Reynolds number is $Re_{\text{pipe}} = 100$. At the nozzle outlet, the Reynolds number based on the nozzle diameter $d_{\text{nozzle}} = 0.06$ m and jet velocity $U_{\text{jet}} = 0.1$ m/s is $Re_{\text{nozzle}} \approx 500$, which is below the usual transition threshold ($Re_{\text{crit}} \approx 400$–$4000$).

Within the pond cavity, the characteristic length is the pond height $H = 0.302$ m, which is the natural hydrodynamic length scale because the domain is periodic in the horizontal direction. With a bulk recirculation velocity of $U_{\text{cavity}} \approx 0.005$ m/s, we obtai $Re_{\text{cavity}} \approx 125$.

These values confirm that the flow remains laminar across the entire domain.

The choice of operating at laminar Reynolds numbers is intentional: the aim of this study is to evaluate a new mixing strategy based on chaotic advection, a mechanism that operates efficiently in laminar regimes and avoids excessive shear that could damage microalgae cells. The objective is therefore not linked to the physical scale of the laboratory setup, but rather to the hydrodynamic regime we seek to investigate.

Importantly, the Reynolds number is the relevant similarity parameter for scaling. Maintaining the same Reynolds number guarantees dynamic similarity across scales. If the characteristic length increases while keeping Re fixed, the required velocity scales as $U \propto \mu Re/(\rho L)$, meaning that larger ponds would require proportionally lower velocities to remain within the laminar regime. This indicates that the proposed chaotic-advection strategy can, in principle, be adapted to larger systems without the need for excessively high inlet velocities.

After analyzing the flow structures across the tested viscosity values (Figure 6), we selected $\mu = 0.012\ Pa.s$ as the representative viscosity for the remainder of the study; this value corresponds to the configuration used in Case Study 1. This value yields a Reynolds number of approximately 100 under our defined geometry and velocity conditions, placing the flow in a transitional regime where both viscous and inertial effects influence mixing. This choice reflects our aim to simulate more demanding flow conditions while remaining realistic. By opting for a more viscous medium, we ensure that our analysis of mixing indicators addresses scenarios where advective transport is less dominant — a critical aspect for systems handling dense or structured suspensions. All subsequent results presented in this paper are based on this selected viscosity.

There are four openings (ES1, ES2, ES3, ES4) located at the connection points between the pond and the piping system. These surfaces are initially treated as walls, but their properties are dynamically updated to act as fluid interfaces when the flow configuration is changed in the pond (Figure 2a). The objective is to define a protocol of connections and mass flows to achieve optimal mixing. To further enhance the mixing process, time-varying mass flow rates can be implemented, allowing greater flexibility in controlling fluid movement within the pond.

At each time step, only two of the four nozzles are active: one functions as an inlet, introducing flow into the pond, while another serves as an outlet, allowing fluid to exit. The remaining two nozzles remain closed, acting as walls. This setup allows for eight valid flow configurations, which can be classified into diagonal flows and lateral flows. Diagonal flows drive fluid from one corner of the pond to the opposite side, promoting cross-pond mixing. On the other hand, lateral flows induce side-to-side circulation, potentially generating localized mixing effects.

The possible flow configurations are summarized in Table IV, where a value of $+1$ represents an inlet, -1 represents an outlet, and 0 indicates that the nozzle remains closed. Initially, there were 12 possible

Table IV: Flow configurations considering symmetry

Configuration	ES1	ES2	ES3	ES4
ES1 $\rightarrow$ ES2	$+1$	-1	0	0
ES1 $\rightarrow$ ES3	$+1$	0	-1	0
ES1 $\rightarrow$ ES4	$+1$	0	0	-1
ES2 $\rightarrow$ ES3	0	$+1$	-1	0
ES2 $\rightarrow$ ES4	0	$+1$	0	-1
ES3 $\rightarrow$ ES4	0	0	$+1$	-1

configurations, each representing a flow from one ES zone (inlet) to another (outlet). However, these configurations form six symmetric pairs, where swapping the inlet and outlet results in a mirrored but structurally identical flow. These pairs share the same absolute values in the matrix but with opposite signs, meaning the overall flow structure remains the same but occurs in the reverse direction. By keeping only one representative from each pair, we reduce the total number of unique configurations to six.

To further enhance the mixing process, these individual flow configurations can be combined in a mixing protocol, where different configurations are applied sequentially or simultaneously to achieve–as fast as possible–a uniform concentration distribution. A mixing protocol can involve alternating between two, three, or even all six configurations over time, allowing a controlled and structured approach to mixing. The goal of such a protocol is to optimize flow patterns—that is, to deliberately structure and manage fluid motion to promote uniform particle distribution, eliminate stagnant zones, enhance circulation efficiency, and limit excessive shear stresses that could harm biological components. This ensures efficient and homogeneous mixing while preserving the integrity of sensitive materials within the pond.

As illustrated in the streamline plots (Figure 7), the flow patterns generated by each configuration reveal how fluid particles are transported and redistributed within the pond. These streamlines represent the stationary state of the flow, providing insight into the persistent structures that govern mixing. Diagonal flows create large-scale circulation structures that sweep fluid across the entire pond, while lateral flows tend to induce more mixing.

The topology of the flow field highlights the presence of specific critical points that govern the organization of streamlines and the underlying mechanisms of chaotic advection. In particular, elliptic points appear at the centers of recirculation vortices, where fluid is trapped and rotates, potentially limiting mixing. Parabolic points, typically located at the walls, correspond to stagnation regions where streamlines are tangent to the boundary, restricting fluid penetration and creating transport barriers. Most importantly, hyperbolic points, where streamlines converge along one axis and diverge along another, play a key role in enhancing chaotic mixing by stretching and folding fluid elements. These saddle points break coherent structures and help redistribute fluid more efficiently across the domain. The interaction between these critical points reorganizes the flow field and promotes the emergence of Lagrangian chaos, a hallmark of effective mixing. Moreover, the use of periodic boundary conditions ensures that fluid parcels exiting one side of the pond

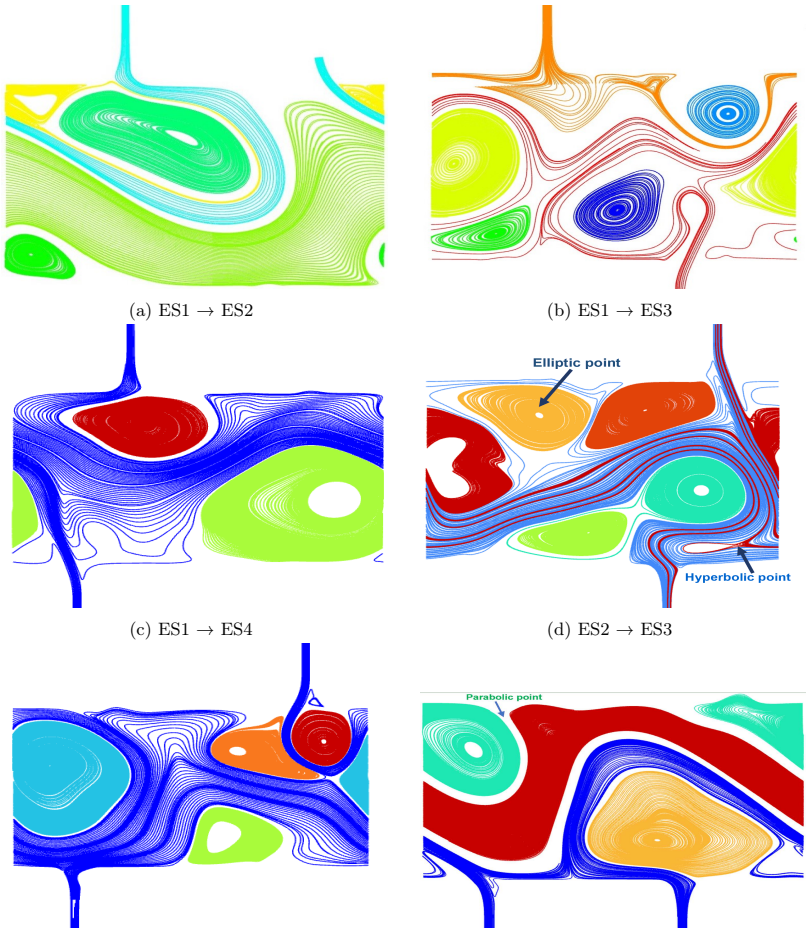

(a) ES1 → ES2 (b) ES1 → ES3

(c) ES1 → ES4 (d) ES2 → ES3

(e) ES2 → ES4 (f) ES3 → ES4

Figure 7: Streamlines of the different flow configurations for steady flows ($Re = 100$, $\rho = 1000\,\mathrm{kg/m^3}$, $\mu = 0.012\,\mathrm{kg/(m \cdot s)}$, $k = 1 \times 10^{-9}\,\mathrm{m^2/s}$). Each color corresponds to a distinct configuration. Key topological features are visible: elliptic points at the centers of recirculation zones (vortices), where fluid rotates; parabolic points near walls, where streamlines are tangent and flow separates or reattaches; and hyperbolic points, where fluid converges along one direction and diverges along another, promoting strong stretching and mixing

re-enter from the opposite side, effectively coupling the behavior of adjacent regions. This prevents mixing from being confined to a single subdomain and allows global circulation structures to emerge, reinforcing the homogenization process.

Alternating between these configurations can improve mixing efficiency and reduce the time required to achieve a uniform concentration distribution. For example, switching between two diagonal flows can help break persistent vortices. Similarly, combining lateral and diagonal flows can introduce flow variations that disrupt stagnant regions and enhance particle dispersion throughout the pond. A practical criterion chosen for switching between configurations is when the fluid has traveled approximately half the pond length, ensuring that the previous flow pattern has sufficiently developed before introducing a new one.

In this work, we present two case studies. Case Study 1 investigates a single inlet–outlet configuration, specifically the diagonal flow path ES3 → ES1, which corresponds to the symmetric counterpart of the second configuration listed in Table IV and Figure 7b. This setup was selected to induce a transverse circulation pattern across the pond, enhancing mixing efficiency. Compared to a straight-through configuration like ES1 → ES2, the diagonal flow promotes stronger interaction with the entire pond cross-section, which is particularly beneficial under high-viscosity conditions.

Case Study 2 explores the effect of alternating between two flow configurations with different durations: the diagonal ES3 → ES1 setup already used in Case Study 1, and ES2 → ES4. This alternation introduces periodic symmetry shifts in the flow pattern, aiming to enhance mixing by disrupting stagnation zones and promoting more uniform scalar dispersion across the domain. The choice of these configurations was informed by the streamline patterns shown in Figure 7, which highlight how ES1 → ES3 and ES2 → ES4 generate strong recirculation zones and avoid flow channeling, while preserving the direction of flow within the connecting tubes—thus minimizing hydraulic transients during switching. These two configurations exhibit a high degree of geometric asymmetry and directional complementarity, both of which are conducive to effective mixing. A comparison of the scalar distribution at the final simulation time between the single-configuration and alternating-configuration scenarios is conducted to evaluate the benefits of dynamic inlet–outlet strategies.

2.4 Mixing Metrics

This section presents the quantitative indicators used to evaluate mixing efficiency based on the evolution of a passive scalar concentration field. Three complementary metrics are considered. First, the concentration variance quantifies the global deviation from spatial homogeneity, providing a direct measure of large-scale mixing. Second, the concentration gradient norm highlights local heterogeneities by measuring the intensity of scalar interfaces, which are key regions for diffusion. Finally, the mix-norm—a negative Sobolev norm—captures both large-scale structures and fine-scale filamentation, making it sensitive to persistent intermediate-scale features that affect scalar dissipation. While flow structure–based metrics such as vortical and stirring length scales can also provide insight into the mechanisms driving mixing (Kalluri and Hillier, 2025), other approaches have been proposed, including topological methods using braids (Thiffeault, 2022; Thiffeault and Finn, 2006) and Lagrangian coherent structures (LCS) (Haller, 2015b; Haller and Yuan, 2000), which focus on identifying dynamically relevant transport barriers and structures. The focus of the present work remains on scalar-based indicators that directly quantify homogenization performance.

2.4.1 Variance of concentration

A classical way to measure mixing is to use the variance of a scalar, which is linked to the L^2 norm of the scalar field. Variance indicates the spread of scalar values and therefore provides a measure of homogeneity in the concentration field (Thiffeault, 2012).

For a discrete scalar quantity φ_i, the variance is defined as:

$$\sigma^2(\varphi_i) = \frac{1}{N}\sum_{n=1}^{N}(\varphi_n^i - \bar{\varphi}^i)^2, \tag{12}$$

where N is the number of elements in the sample, φ_n^i is the scalar value at the n-th sample, and $\bar{\varphi}^i$ is the sample mean. This discrete variance quantifies the fluctuation of each sample around the mean.

In the continuous case, the variance over a spatial domain Ω is defined as:

$$\sigma^2(\varphi) = \int_\Omega \left(\varphi(t,x) - \bar{\varphi}(t)\right)^2 dx, \tag{13}$$

where $\bar{\varphi}(t)$ is the spatial average of φ at time t, given by:

$$\bar{\varphi}(t) = \frac{1}{|\Omega|}\int_\Omega \varphi(t,x)\, dx. \tag{14}$$

To investigate how the scalar variance evolves over time in a physical system, we consider the classical advection-diffusion problem described by Eq. (3) with the same boundary conditions:

$$\begin{cases} \partial_t\varphi + \vec{u}\cdot\nabla\varphi &= k\Delta\varphi \quad \text{in } \Omega, \\ \partial_{\vec{n}}\varphi &= 0 \quad \text{on } \partial\Omega, \\ \varphi|_{t=0} &= \varphi_0(x) \quad \text{in } \Omega, \end{cases} \tag{15}$$

where Ω is a bounded open set of $\mathbb{R}^d$ with Lipchitz boundary $\partial\Omega$ whose outward unitary normal is denoted by $\vec{n}$. In addition, the velocity field $\vec{u}$ is assumed to satisfy the incompressibility of the fluid:

$$\operatorname{div}\vec{u} = 0 \text{ in } \Omega \text{ and } \vec{u}\cdot\vec{n} = 0 \text{ on } \partial\Omega.$$

Using then that $\vec{u}\cdot\nabla\varphi = \operatorname{div}(\vec{u}\varphi)$, we obtain:

$$\begin{aligned} \partial_t\left(\int_\Omega \varphi(t,x)\, dx\right) &= \int_\Omega \operatorname{div}\left(k\nabla\varphi - \vec{u}\varphi\right) dx \\ &= \int_{\partial\Omega} k\partial_{\vec{n}}\varphi\,\varphi - \vec{u}\cdot\vec{n}\varphi\, dS = 0, \end{aligned}$$

and thus:

$$\int_\Omega \varphi(t,x)\, dx = \int_\Omega \varphi_0(x)\, dx. \tag{16}$$

Assuming now that $\varphi(t,.)$ weakly converges toward some $\varphi_\infty(.)$ in $L^2(\Omega)$ as $t \to +\infty$, we obtain from Eq. (16):

$$\int_\Omega \varphi_\infty\, dt = \int_\Omega \varphi_0(x)\, dx. \tag{17}$$

It is worth noting that φ_∞ is also the unique solution to the steady-state problem associated to Eq. (15) which reads as:

$$\begin{cases} \vec{u}\cdot\nabla\varphi_\infty &= k\Delta\varphi_\infty \quad \text{in } \Omega, \\ \partial_{\vec{n}}\varphi_\infty &= 0 \quad \text{on } \partial\Omega. \end{cases} \tag{18}$$

As a result, φ_∞ is the spatial average of φ_0.

Let $\varphi(t,x)$ denote the concentration field, and define the deviation from the uniform state as $\varphi(t,x) - \varphi_\infty$, where φ_∞ is the spatially uniform equilibrium concentration. We aim to compute the rate at which this deviation converges to zero as $t \to \infty$.

We define the deviation from the asymptotic concentration as $\theta = \varphi - \varphi_\infty$. Substituting this into Eq. (15) and using (18), we obtain the governing equation for θ:

$$\begin{cases} \partial_t \theta + \vec{u} \cdot \nabla \theta &= k \Delta \theta & \text{in } \Omega, \\ \partial_{\vec{n}} \theta &= 0 & \text{on } \partial\Omega, \\ \theta|_{t=0} &= \theta_0(x) - \theta_\infty & \text{in } \Omega. \end{cases} \tag{19}$$

Multiplying Eq. (19) by θ and using Green's formula, we obtain:

$$\frac{1}{2}\partial_t \int_\Omega \theta^2 \, dx = -k \int_\Omega |\nabla \theta|^2 \, dx - \int_\Omega \vec{u} \cdot \nabla \theta \, \theta \, dx. \tag{20}$$

Using Green's formula one more time together with $\mathrm{div}(\vec{u}) = 0$, we have:

$$\begin{aligned} \int_\Omega \vec{u} \cdot \nabla \theta \, \theta \, dx &= \int_{\partial\Omega} \vec{u} \cdot \vec{n} \, \theta^2 \, dS - \int_\Omega \theta \, \mathrm{div}\,(\vec{u}\theta) \, dx \\ &= \int_{\partial\Omega} \vec{u} \cdot \vec{n} \, \theta^2 \, dS - \int_\Omega \theta \left(\underbrace{\mathrm{div}\,(\vec{u})}_{=0} \theta + \vec{u} \cdot \nabla \theta \right) dx, \end{aligned}$$

and thus

$$\int_\Omega \vec{u} \cdot \nabla \theta \, \theta \, dx = \frac{1}{2} \int_{\partial\Omega} \vec{u} \cdot \vec{n} \, \theta^2 \, dS = 0. \tag{21}$$

Denoting by $\|\psi\|_{L^2(\Omega)} = \left(\int_\Omega \psi^2(x) \, dx\right)^{1/2}$ the L^2- norm of ψ, we obtain the following equality:

$$\frac{1}{2}\partial_t \|\theta(t,.)\|^2_{L^2(\Omega)} = -k \|\nabla \theta(t,.)\|^2_{L^2(\Omega)}. \tag{22}$$

To get a bound on the L^2-norm of θ, we now use the Poincaré-Wirtinger inequality which holds for any $\psi \in H^1(\Omega)$ satisfying $\int_\Omega \psi(x) \, dx = 0$ and reads as:

$$\|\psi\|_{L^2(\Omega)} \leq C_P \|\nabla \psi\|_{L^2(\Omega)} \tag{23}$$

Using Eq. (23) together with Eq. (22), we get:

$$\partial_t \|\theta(t,.)\|^2_{L^2(\Omega)} \leq -\frac{2k}{C_p^2} \|\theta(t,.)\|^2_{L^2(\Omega)} \tag{24}$$

which, noting $h(t) = \|\theta(t,.)\|^2_{L^2(\Omega)}$, can be recast as:

$$\partial_t \left(e^{\frac{2tk}{C_P^2}} h(t) \right) \leq 0. \tag{25}$$

Integrating the previous inequality over the interval $[0, t]$ then yields:

$$h(t) \leq h(0) e^{-\frac{2tk}{C_P^2}}. \tag{26}$$

Since $\theta = \varphi - \varphi_\infty$, we finally infer:

$$\|\varphi(t,.) - \varphi_\infty\|_{L^2(\Omega)} \leq \|\varphi_0 - \varphi_\infty\|_{L^2(\Omega)} \exp\left(-\frac{kt}{C_P^2}\right). \tag{27}$$

Noting that φ_∞ is the mean value of φ over Ω. With the previous estimate we obtain that the variance of the concentration decays exponentially with time:

$$\sigma^2(\varphi) \propto \exp\left(-\frac{kt}{C_P^2}\right). \tag{28}$$

Remark 1. The unit of k is $[m^2/s]$ and the one of the Poincaré constant C_P is $[m]$. Therefore kt/C_p^2 is a dimensionless parameter. It can be related to the Péclet number $\mathrm{Pe} = LU/k$ with U, L being respectively a characteristic velocity and length by

$$\frac{kt}{L^2} = \frac{k}{UL}\frac{tU}{L} = \frac{1}{\mathrm{Pe}}\hat{U}, \tag{29}$$

with $\hat{U} = (U)/(L/t)$ is a dimensionless characteristic velocity.

Two key observations can be made from the estimate in Eq. (28). First, the role of the velocity field $\vec{u}$ in mixing the scalar φ is not evident, as the estimate remains valid even when the velocity field is zero. This suggests that the variance primarily reflects the effect of diffusion on the mixing rate. Second, when the Péclet number is large or the diffusivity k is small, the variance may decay very slowly as $t \to \infty$, indicating slow convergence toward a uniform concentration.

Remark 2. The result in Eq. (28) remains valid even when $\varphi_\infty \neq \bar{\varphi}^i$, i.e., when the asymptotic state is not spatially uniform. This situation arises, for example, in domains with inhomogeneous Dirichlet boundary conditions on part of $\partial\Omega$, which lead to a non-constant stationary solution φ_∞. In such cases, although φ_∞ differs from the spatial average of the initial condition, the decay estimate still holds provided a Poincaré inequality can be established for the deviation $\theta = \varphi - \varphi_\infty$. This is ensured, for instance, when the velocity field satisfies the no-slip condition ($\vec{u} = 0$) on the boundary and the scalar field θ satisfies a homogeneous Dirichlet condition on a portion of $\partial\Omega$. Under these assumptions, the usual functional inequality applies, and the derivation leading to Eq. (28) remains valid.

Another non-uniform mixing scenario is also discussed in Thiffeault (2021) (see Section V.A) where the mean concentration is conserved for all times but $\varphi_\infty \neq \overline{\varphi_0}(t)$. Note that this example lacks a uniquely defined stationary solution due to unspecified initial condition but once an initial condition is given, such example fits into the present framework. Thus, the decay estiimate in Eq. (28) is valid

As shown by the decay estimate, the rate at which variance decreases is greatly influenced by the diffusivity k and the domain. This insight is crucial for optimizing mixing processes, particularly in contexts where efficient and uniform distribution of components is essential. For large Peclet numbers or low diffusivity k, the variance converges slowly, reflecting the dependence of mixing efficiency on these parameters. In this paper, we use variance to quantify how concentration values deviate from the mean.

2.4.2 Concentration gradient

We compute the evolution of the gradient of $\varphi(t,x)$ satisfying the advection-diffusion Eq. (19). First, we denote $w_i = \partial_i\varphi$ and compute the derivative of (19), which yields:

$$\partial_t\partial_i\varphi + \partial_i(u_j\partial_j\varphi) = k\Delta\partial_i\varphi \quad \text{in } \Omega. \tag{30}$$

Using the identity $\partial_i(u_j\partial_j\varphi) = \partial_i u_j\,\partial_j\varphi + u_j\,\partial_j\partial_i\varphi$ and recognizing that $\nabla\vec{u} = (\partial_i u_j)_{i,j}$, we obtain:

$$\partial_i(u_j\partial_j\varphi) = \nabla\vec{u}\,\vec{w} + (\vec{u}\cdot\nabla)\vec{w}. \tag{31}$$

Thus, the gradient of concentration $\vec{w} = \nabla\varphi$ satisfies:

$$\partial_t\vec{w} + \nabla\vec{u}\,\vec{w} + (\vec{u}\cdot\nabla)\vec{w} = k\Delta\vec{w} \quad \text{in } \Omega. \tag{32}$$

Taking the inner product of Eq. (32) with $\vec{w}$ and integrating over Ω, we obtain:

$$\frac{1}{2}\partial_t\|\vec{w}\|^2_{L^2(\Omega)} = -k\sum_{i=1}^{d}\left(-\int_{\partial\Omega}\partial_{\vec{n}}w_i\,w_i\,d\sigma + \int_\Omega|\nabla w_i|^2\,dx\right)$$

$$+\frac{1}{2}\int_{\partial\Omega}\vec{u}\cdot\vec{n}\,|\vec{w}|^2\,d\sigma-\int_{\Omega}\nabla\vec{u}\,\vec{w}\cdot\vec{w}\,dx,$$

where we have used the identity:

$$\int_{\Omega}((\vec{u}\cdot\nabla)\vec{w})\cdot\vec{w}\,dx=\frac{1}{2}\int_{\partial\Omega}\vec{u}\cdot\vec{n}\,|\vec{w}|^2\,d\sigma. \tag{33}$$

This identity can be derived from Green's formula as follows:

$$\int_{\Omega}((\vec{u}\cdot\nabla)\vec{w})\cdot\vec{w}\,dx=\int_{\Omega}u_i(\partial_i w_j)w_j\,dx=\int_{\partial\Omega}\vec{u}\cdot\vec{n}\,|\vec{w}|^2\,d\sigma-\int_{\Omega}\mathrm{div}(\vec{u})|\vec{w}|^2+((\vec{u}\cdot\nabla)\vec{w})\cdot\vec{w}\,dx.$$

Using the condition $\mathrm{div}(\vec{u})=0$, we obtain the previously mentioned formula. Since $\vec{u}\cdot\vec{n}=0$ on the boundary, we finally obtain:

$$\frac{1}{2}\partial_t\|\vec{w}\|^2_{L^2(\Omega)}=-k\sum_{i=1}^{d}\int_{\Omega}|\nabla w_i|^2\,dx-\int_{\Omega}\nabla\vec{u}\,\vec{w}\cdot\vec{w}\,dx+k\sum_{i=1}^{d}\int_{\partial\Omega}\partial_{\vec{n}}w_i\,w_i\,d\sigma. \tag{34}$$

Assuming that the boundary term vanishes in the above equation (see Remark 3 below), we obtain the evolution of the variance of the concentration gradient:

$$\frac{1}{2}\partial_t\|\vec{w}\|^2_{L^2(\Omega)}=-k\sum_{i=1}^{d}\int_{\Omega}|\nabla w_i|^2\,dx-\int_{\Omega}\nabla\vec{u}\,\vec{w}\cdot\vec{w}\,dx, \tag{35}$$

which is similar to (Thiffeault, 2012, Eq. (3.13)). The strain-rate tensor is:

$$S(\vec{u})=\frac{1}{2}\left(\nabla\vec{u}+\nabla\vec{u}^T\right), \tag{36}$$

and Eq. (35) can finally be expressed as:

$$\frac{1}{2}\partial_t\|\vec{w}\|^2_{L^2(\Omega)}=-k\sum_{i=1}^{d}\int_{\Omega}|\nabla w_i|^2\,dx-2\int_{\Omega}S(\vec{u})\vec{w}\cdot\vec{w}\,dx. \tag{37}$$

Eq. (37) describes the time evolution of the variance of the concentration gradient $\vec{w}=\nabla\varphi$ within the domain Ω. The first term on the right-hand side represents diffusive dissipation, which always acts to reduce the gradient magnitude. The second term quantifies the influence of velocity gradients, through the strain-rate tensor $S(\vec{u})$, on the amplification or attenuation of the concentration gradients. As such, this formulation is useful for characterizing and quantifying the effectiveness of mixing in fluid systems.

Remark 3. To establish Eq. (35), we required that the boundary term in the intermediate expression vanish. This is automatically satisfied under certain standard conditions:

- periodic boundary conditions,
- Dirichlet conditions such that $w_i|_{\partial\Omega}=0$,
- or Neumann-type conditions where $\partial_{\vec{n}}w_i=0$.

Since $\vec{w}=\nabla\varphi$, we can consider the boundary condition on φ. If φ satisfies a homogeneous Neumann boundary condition $\partial_{\vec{n}}\varphi=0$, then:

$$\vec{n}\cdot\nabla\varphi=\vec{n}\cdot\vec{w}=0,$$

i.e., the normal component of $\vec{w}$ vanishes on $\partial\Omega$. However, this is not sufficient to guarantee that the full boundary term $\sum_{i=1}^{d} \int_{\partial\Omega} \partial_{\vec{n}} w_i \, w_i \, d\sigma$ is zero, because it involves normal derivatives of the tangential components of $\vec{w}$. Specifically, this term reduces to:

$$\sum_{i=1}^{d} \int_{\partial\Omega} \partial_{\vec{n}} w_i \, w_i \, d\sigma = \sum_{j=1}^{d-1} \int_{\partial\Omega} (\partial_{\vec{n}} \vec{w} \cdot \vec{t}_j)(\vec{w} \cdot \vec{t}_j) \, d\sigma, \tag{38}$$

where $\vec{t}_j$ is a local orthonormal basis of the tangent plane to the boundary. The purpose of including Eq. (38) is to make this structure of the boundary term explicit. It shows that even if the normal component of $\vec{w}$ vanishes, we must still assume or ensure that either:

- the tangential components of $\vec{w}$ vanish,
- or their normal derivatives vanish on $\partial\Omega$,

in order for the boundary term to vanish. Therefore, Eq. (38) helps clarify that the vanishing of the boundary term cannot be concluded solely from $\vec{n} \cdot \vec{w} = 0$, and motivates the assumption (made in deriving Eq. (35)) that the boundary term is zero under suitable additional conditions. Moreover, this term is multiplied by the molecular diffusivity k, which is very small in our system, further justifying its neglect.

2.4.3 Mix norm

The mix norm is defined as:

$$\|\varphi\|_m := \|\nabla\psi\|_{L^2(\Omega)}, \quad \text{where } \psi \in H_0^1(\Omega) \text{ satisfies } -\Delta\psi = \varphi - \varphi_\infty \text{ in } \Omega, \ \psi = 0 \text{ on } \partial\Omega. \tag{39}$$

Here, φ_∞ denotes the spatial average of φ over Ω. For notational convenience, we recall that $\theta = \varphi - \varphi_\infty$ throughout this section.

Remark 4. Numerically, the Poisson equation in Eq. (39) is solved by introducing an auxiliary scalar field governed by a diffusion-type equation with a source term $(\varphi - \varphi_\infty)$. The source term is implemented as a piecewise constant field, computed from the local scalar concentration minus its spatial mean. This field is stored and updated during the simulation to enable consistent evaluation of the mix-norm functional. The mix-norm is then evaluated as $\|\varphi\|_m = \|\nabla\psi\|_{L^2(\Omega)}$.

The mix norm satisfies the following properties. For any $q \in H_0^1(\Omega)$, we have:

$$\int_\Omega -\Delta\psi \, q \, dx = \int_\Omega (\varphi - \varphi_\infty) q \, dx, \tag{40}$$

which, by integration by parts, yields:

$$\int_\Omega \nabla\psi \cdot \nabla q \, dx = \int_\Omega \theta q \, dx. \tag{41}$$

Setting $q = \psi$ gives:

$$\|\varphi\|_m^2 = \int_\Omega \theta\psi \, dx. \tag{42}$$

Setting $q = \theta$ gives:

$$\|\theta\|_{L^2(\Omega)}^2 = \int_\Omega \nabla\psi \cdot \nabla\theta \, dx. \tag{43}$$

To provide a spectral characterization of the mix norm, we consider $\lambda_j > 0$ and $\psi_j \in L^2(\Omega)$ as the orthonormal basis of $L^2(\Omega)$ composed of eigenfunctions of the (self-adjoint) operator $-\Delta$ with domain $H_0^1(\Omega)$. Hence:

$$-\Delta\psi_j = \lambda_j\psi_j \text{ in } \Omega,\ \psi_j|_{\partial\Omega} = 0.$$

In addition, we assume that the eigenvalues are ordered as $\lambda_1 < \lambda_2 < \cdots$.

Writing $\theta = \varphi - \varphi_\infty$ as:

$$\theta = \sum_j (\theta, \psi_j)_{L^2(\Omega)}\, \psi_j,$$

we obtain that ψ satisfying (39) can be expressed as:

$$\psi = \sum_j \frac{(\theta, \psi_j)_{L^2(\Omega)}}{\lambda_j}\psi_j.$$

Since $(\nabla\psi_j, \nabla\psi_l)_{L^2(\Omega)} = \lambda_j\delta_{jl}$, we obtain:

$$\|\varphi\|_m^2 = \|\nabla\psi\|_{L^2(\Omega)}^2 = \sum_j \frac{(\theta, \psi_j)_{L^2(\Omega)}^2}{\lambda_j}, \tag{44}$$

which indicates that the mix norm receives its most significant contributions from the components of θ associated with the small eigenvalues.

Finally, we get that:

$$\|\varphi\|_m^2 \le \frac{1}{\lambda_1}\sum_j (\theta, \psi_j)_{L^2(\Omega)}^2 = \frac{1}{\lambda_1}\|\theta\|_{L^2(\Omega)}^2, \tag{45}$$

showing that the decay of the mix norm is bounded by the decay of the variance.

Remark 5. The purpose of this remark is to show that the estimate (45) can be obtained without resorting to spectral decomposition. Using Eq. (43) together with the Poincaré–Wirtinger inequality, we obtain:

$$\begin{aligned}
\|\varphi(t,.)\|_m^2 &= \int_\Omega \left(\varphi(t,.) - \varphi_\infty\right)\psi\, dx \\
&\le \|\varphi(t,.) - \varphi_\infty\|_{L^2(\Omega)}\, \|\psi\|_{L^2(\Omega)} \\
&\le C_P\, \|\varphi(t,.) - \varphi_\infty\|_{L^2(\Omega)}\, \|\nabla\psi\|_{L^2(\Omega)} \\
&\le C_P\, \|\varphi(t,.) - \varphi_\infty\|_{L^2(\Omega)}\, \|\varphi(t,.)\|_m .
\end{aligned}$$

Using then (27), we obtain the mixing norm decay:

$$\|\varphi(t,.)\|_m \le C_P\, \|\varphi_0 - \varphi_\infty\|_{L^2(\Omega)} \exp\left(-\tfrac{kt}{C_P^2}\right). \tag{46}$$

We now compute the time-variation of the mixing norm of $\varphi(t,x)$ satisfying (19). Taking the time derivative of $\|\varphi(t,.)\|_m^2$ yields:

$$\begin{aligned}
\partial_t \|\varphi(t,.)\|_m^2 &= 2\int_\Omega \partial_t\nabla\psi\cdot\nabla\psi\, dx \\
&= 2\int_{\partial\Omega} \partial_{\vec{n}}\partial_t\psi\, \psi\, d\sigma - 2\int_\Omega \mathrm{div}\left(\partial_t\nabla\psi\right)\, \psi\, dx \\
&= 2\int_\Omega \partial_t(\varphi - \varphi_\infty)\, \psi\, dx \\
&= 2\int_\Omega \mathrm{div}\left(k\nabla\theta - \vec{u}\theta\right)\, \psi\, dx \\
&= 2\int_{\partial\Omega} \left(k\nabla\theta\cdot\vec{n} - \vec{u}\cdot\vec{n}\theta\right)\, \psi\, d\sigma - 2\int_\Omega k\nabla\theta\cdot\nabla\psi - \theta\,\vec{u}\cdot\nabla\psi\, dx.
\end{aligned}$$

Using then Eq. (43), we obtain:

$$\partial_t \|\varphi(t,.)\|_m^2 = -2k \|\varphi(t,.) - \varphi_\infty\|_{L^2(\Omega)}^2 - 2\int_\Omega (\varphi - \varphi_\infty)\, \vec{u} \cdot \nabla\psi \, dx. \tag{47}$$

Remark 6. The classical definition of the mix norm employs a Neumann boundary condition on ψ. We define:

$$\|\varphi\|_{m,\text{classical}} := \|\nabla\psi\|_{L^2(\Omega)} \tag{48}$$

where $\psi \in L_0^2(\Omega)$ (i.e., the space of square-integrable functions with zero mean over Ω) satisfies:

$$-\Delta\psi = \varphi - \varphi_\infty \quad \text{in } \Omega, \tag{49}$$

$$\partial_{\vec{n}}\psi = 0 \quad \text{on } \partial\Omega. \tag{50}$$

The function ψ is well-defined since $\int_\Omega (\varphi - \varphi_\infty)\, dx = 0$. However, all the key mathematical properties of the mixing norm are preserved when using the Dirichlet condition $\psi|_{\partial\Omega} = 0$ instead, allowing for equivalent analysis and interpretation.

Formally taking $k = 0$ in Eq. (47), we obtain:

$$\partial_t \|\varphi(t,.)\|_m^2 = -2\int_\Omega (\varphi - \varphi_\infty)\, \vec{u} \cdot \nabla\psi \, dx, \tag{51}$$

which is consistent with the purely advective case found in the literature (Zhu et al., 2024).

The time derivative expression in Eq. (47) provides a rigorous characterization of how mixing evolves in time, combining both diffusive and advective effects. The first term, $-2k \|\varphi(t,.) - \varphi_\infty\|_{L^2(\Omega)}^2$, directly reflects the smoothing effect of diffusion, promoting decay of concentration variance. The second term, $-2\int_\Omega (\varphi - \varphi_\infty)\, \vec{u} \cdot \nabla\psi \, dx$, captures the contribution of advection by the velocity field $\vec{u}$, which may either enhance or suppress the decay depending on the alignment of $\vec{u}$ with concentration gradients.

The mix norm, Eq. (39), emphasizes the large-scale inhomogeneities of the scalar field $\varphi - \varphi_\infty$. As shown in the spectral representation, the small eigenvalues λ_j dominate the mix norm, implying that it is especially sensitive to low-frequency (large-scale) features in the concentration field. This is in contrast with variance-based norms, which weigh all modes equally. This selective sensitivity makes the mix norm a more appropriate tool in situations where persistent large-scale heterogeneities are of concern (Mathew et al. (2005), Thiffeault (2012), Zhu et al. (2024)).

3 Results

This section presents the main findings of our study and is divided into two parts. The first subsection offers a visual inspection of the flow and scalar concentration patterns over time, providing qualitative insight into the dynamics of mixing. The second subsection quantifies these observations through the above described evolution of mixing metrics, offering a more rigorous assessment of mixing performance.

3.1 Flow Visual Analysis and Scalar Patterns

3.1.1 Case Study 1: ES3 → ES1

The temporal evolution of the scalar concentration field in the ES3 → ES1 configuration (Figure 8) reveals key stages in the transition from an initially segregated distribution to a well-mixed state, governed by the interplay of advection and diffusion. At the early stage ($t = 40$ s), the scalar field remains structured, with distinct high- and low-concentration zones extending laterally across the domain. These zones are reminiscent of the initial condition and exhibit minimal distortion, indicating that large-scale advective

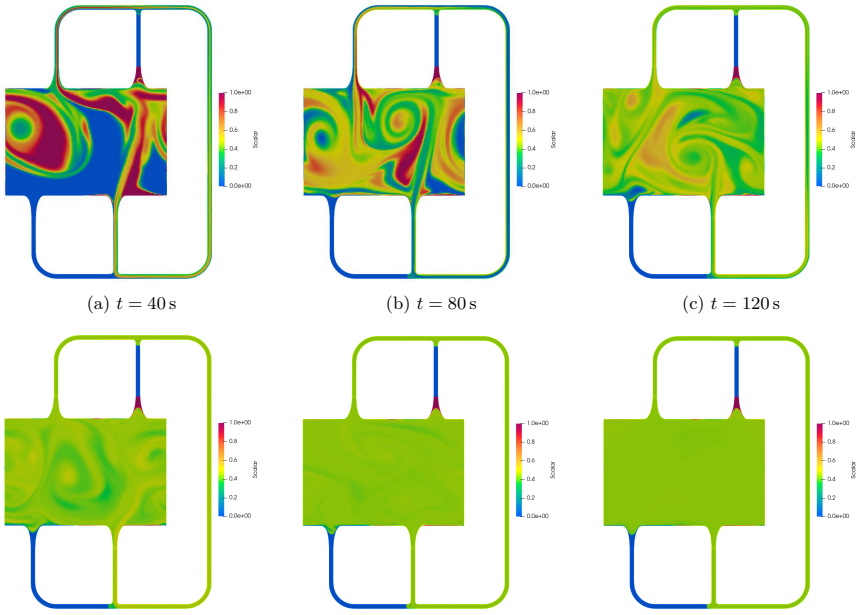

(a) $t = 40\,\mathrm{s}$ (b) $t = 80\,\mathrm{s}$ (c) $t = 120\,\mathrm{s}$

(d) $t = 160\,\mathrm{s}$ (e) $t = 200\,\mathrm{s}$ (f) $t = 240\,\mathrm{s}$

Figure 8: Scalar patterns for case study 1: ES3 → ES1 at Re = 100 with flow times of 40s, 80s, 120s, 160s, 200s, and 240s under continuous flow conditions

mixing has not yet taken hold. Weak vortical features are observed primarily near the jet inlets on the left-hand side, but their influence is localized, and the overall scalar stratification remains largely intact. Sharp scalar gradients persist, particularly near the center of the pond, where diffusion alone is insufficient to erode the initial concentration boundaries.

At $t = 120$ s, the scalar distribution exhibits a visibly higher degree of homogenization. Coherent vortices have lost their initial integrity, giving way to increasingly disordered scalar structures with a broader spectrum of concentration values. This is indicative of a transition toward the diffusion-dominated regime, where advection has sufficiently stirred the scalar field to allow diffusion to smooth residual concentration differences. The domain is now populated by fragmented filaments and irregular patches of scalar, particularly in regions away from the jet core, signifying the waning dominance of large-scale advective transport. As the simulation progresses to $t = 160$ s, the scalar field continues to evolve toward uniformity. The dominant features now consist of intermediate concentrations with only faint gradients separating them. Residual heterogeneities are confined to zones of weaker flow intensity—particularly corners and lateral regions—where recirculatory dynamics may trap scalar-rich fluid and delay homogenization. At $t = 200$ s and $t = 240$ s, these zones gradually diminish, and the scalar field approaches a near-equilibrium distribution. Although complete uniformity is not achieved, the remaining concentration gradients are shallow and spatially diffuse, suggesting that the combined effects of sustained advection and molecular diffusion have significantly reduced scalar variance. This evolution illustrates the transition from advection-dominated to diffusion-driven mixing: large-scale jet vortices first stretch and fold the scalar field, increasing interfacial area, while at later stages diffusion smooths the finer gradients left by the breakdown of coherent structures (Dimotakis, 2005).

3.1.2 Case Study 2: alternation between configurations C1 (ES3 → ES1) and C2 (ES2 → ES4)

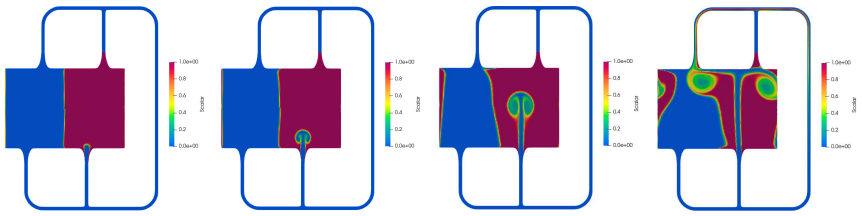

(a) 3 s (b) 5 s (c) 10 s (d) 20 s

Figure 9: Temporal progression of the jet propagation for different times after activation

In the second case study, the inlet and outlet positions were switched every $\tau = 20\,\mathrm{s}$ of real time. This switching interval was chosen to ensure that each inlet/outlet configuration has sufficient time to contribute effectively to the flow development. Numerical observations, illustrated in Fig. 9, show the temporal progression of the jet at 3, 5, 10, and 20 s. These snapshots highlight that the jet requires several advection times to propagate, expand, and generate coherent recirculation structures that influence the scalar field. Switching too early (e.g., after only 3–5 s) would interrupt the formation and transport of these structures, reducing the benefit of alternating actuation. Therefore, $\tau = 20\,\mathrm{s}$ was selected as a physically relevant circulation timescale that allows the jet-induced structures to fully develop and interact with the passive scalar before the flow configuration changes.

The evolution of the scalar concentration field under the alternating jet sequence (C1: ES3 → ES1 and

C2: ES2 → ES4) (Figure 10) shows a noticeably different mixing behavior compared to the single diagonal steady forcing (ES3 → ES1) seen earlier. Already at $t = 40\,\mathrm{s}$, the scalar field starts to show early signs of disruption over a broader area. Instead of the large, coherent vortices dominating the center—as was typical with the diagonal setup—the concentration patterns here are finer and more fragmented, with thin filaments stretched in multiple directions. This suggests that the changing jet orientations are quickly stretching and folding the scalar, creating more complex structures and accelerating the breakdown of the initial gradient. By $t = 80\,\mathrm{s}$, the scalar field looks even more tangled, with filaments extending further

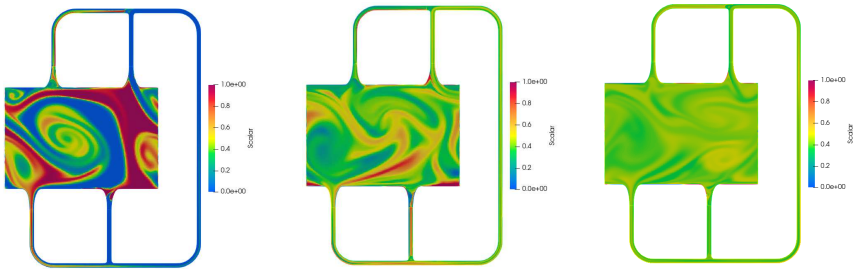

(a) $t = 40\,\mathrm{s}$, Alternation 1 (b) $t = 80\,\mathrm{s}$, Alternation 2 (c) $t = 120\,\mathrm{s}$, Alternation 3

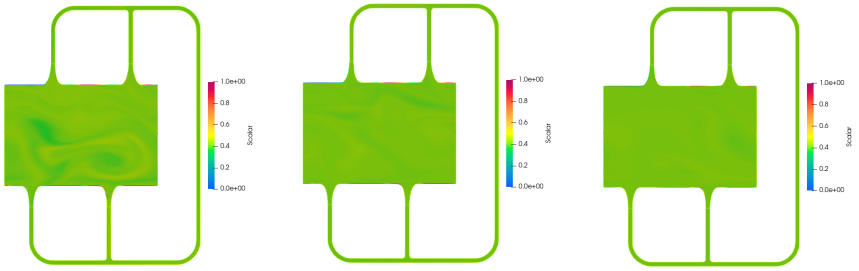

(d) $t = 160\,\mathrm{s}$, Alternation 4 (e) $t = 200\,\mathrm{s}$, Alternation 5 (f) $t = 240\,\mathrm{s}$, Alternation 6

Figure 10: Scalar concentration patterns for Case Study 2: alternation between configurations C1 (ES3 → ES1) and C2 (ES2 → ES4), at Re = 100 with flow times of 40s, 80s, 120s, 160s, 200s, and 240s under continuous flow conditions

across the domain, including into the side channels and corners. In contrast to the fixed jets, where strong mixing was mainly limited to the central region, the alternating setup manages to push scalar deeper into areas that were previously left more isolated. This shows that the switching helps energize not just the core flow but also the slower-moving zones near the walls. At $t = 120\,\mathrm{s}$, the scalar field continues to even out. The sharp filaments seen earlier have mostly smoothed out, leaving a more uniform concentration across the domain. Compared to the fixed jet configuration, the alternating strategy clearly speeds up the transition from structured filaments to smoother, diffusion-dominated mixing. Notably, by $t = 160\,\mathrm{s}$, the scalar field in Case 2 is already approaching a well-mixed state, with high spatial uniformity and only minor residual concentration gradients remaining near the boundaries. The structured filaments that were prominent

at earlier times have largely dissipated, giving way to a smoother field indicative of diffusion-dominated mixing. This early transition stands in contrast to Case 1, where at the same time point, discernible filamentary structures persist in several regions, particularly in the corners and side zones, signaling that advective stretching and homogenization are still ongoing. By $t = 200\,\mathrm{s}$ and $t = 240\,\mathrm{s}$, both configurations ultimately reach similar levels of mixing, with scalar distributions that are nearly flat across the entire domain. However, the key distinction lies in the rate of convergence: in Case 2, the homogenization process is essentially complete by $t = 160\,\mathrm{s}$, indicating a faster transition from advection-dominated to diffusion-dominated regimes. In contrast, Case 1 requires additional time for the remaining scalar structures to break down and redistribute.

Compared to the fixed diagonal jets where mixing starts strong but tends to stay confined, the alternating strategy introduces enough variability to break up the scalar field faster and across a larger area. This behavior fits well with the idea of chaotic advection, where regularly changing the flow pathlines helps particles avoid getting trapped in stagnant zones.

3.2 Evolution of Mixing Metrics

3.2.1 Variance of Concentration

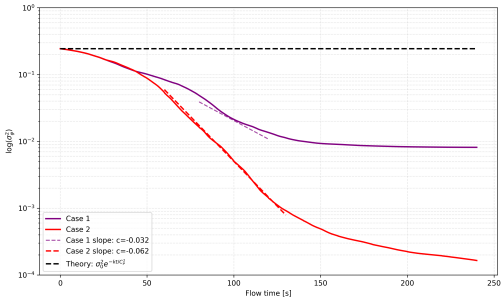

Figure 11: Evolution of scalar variance σ_φ^2 for Case Study 1 and Case Study 2 on a semi-logarithmic scale, compared with the theoretical decay predicted by pure diffusion

In both configurations, the concentration variance σ_φ^2 decreases monotonically over time (Figure 11), indicating progressive scalar homogenization. However, the rate and extent of this decline differ markedly. In Case 2, the variance decays more rapidly and ultimately reaches an order-of-magnitude lower than in Case 1 by $t = 240\,\mathrm{s}$, highlighting a substantially more effective mixing process. This enhanced performance reflects more vigorous scalar stretching and interfacial renewal, which accelerate diffusive homogenization through increased interfacial area, as emphasized by Dimotakis (2005); Ottino (1989). The logarithmic decay regime observed in Case 2 aligns with the mechanisms of efficient scalar filamentation described by Thiffeault (2012). In contrast, the variance plateau in Case 1 beyond $t \approx 150\,\mathrm{s}$ suggests the persistence of weakly deformed regions or coherent structures that inhibit further homogenization. The diminished decay rate in this regime points to a transition where diffusive mixing is no longer supported by sufficient advective stirring.

To further emphasize the efficiency of the imposed flow protocol, we compare the variance decay in Case 2 with the theoretical decay expected from pure molecular diffusion, obtained from the same initial condition

without any advective motion (Figure 11). While diffusion alone leads to a very slow, near-exponential decrease in variance, the active flow in Case 2 accelerates homogenization by over an order of magnitude. At $t = 240, \mathrm{s}$, the variance in the purely diffusive scenario remains above 10^{-2}, whereas Case 2 reaches values near 10^{-4}.

These observations collectively support the conclusion that Case 2 provides a flow environment where scalar transport is accelerated both through faster stretching of concentration gradients and through more effective disruption of coherent structures that typically slow down mixing. The interplay between rapid initial stretching and sustained small-scale diffusive action in Case 2 contrasts with the slower, structurally constrained mixing observed in Case 1. This distinction is critical because it indicates that the efficiency of mixing is not governed solely by the initial energy input or flow speed, but by the ability of the flow to sustain fine-scale deformation over time, as outlined in recent advances in chaotic and turbulent mixing theory (Cant, 2001; Thiffeault, 2012).

3.2.2 Concentration Gradient

The time evolution of the concentration gradient norm $||\nabla\varphi||_{L^2}$ offers a global measure of scalar interface sharpness, reflecting the interplay between advective stretching and diffusive smoothing. As shown in Figure 12, both cases initially exhibit similar behavior during the first 20 s, when identical inlet–outlet boundary conditions promote comparable stretching dynamics. During this phase, scalar gradients grow as the imposed flow begins to distort the initially smooth concentration field.

Following the switching of inlet and outlet at $t = 20\,\mathrm{s}$, distinct dynamics emerge. In Case 2, a short-lived dip appears around $t \approx 25\,\mathrm{s}$, indicating a transient realignment of the scalar field as newly formed shear layers partially flatten pre-existing interfaces before filamentation resumes. This behavior reflects an intermediate restructuring stage, where flow re-organization temporarily suppresses gradient intensity prior to more vigorous interfacial deformation.

After this dip, Case 2 exhibits a more pronounced and delayed peak in $||\nabla\varphi||_{L^2}$, reaching a significantly higher amplitude around $t \approx 55\,\mathrm{s}$. This behavior indicates stronger and more sustained scalar stretching, likely associated with enhanced Lagrangian deformation and alignment of scalar interfaces with regions of high strain. By contrast, Case 1 reaches its peak earlier and at a lower value, followed by a more gradual decline, consistent with stirring dominated by less dynamic large-scale structures.

The subsequent plateau in Case 1 suggests stagnation in gradient amplification, likely due to the persistence of coherent vortices or low-shear zones that limit further interfacial sharpening. In contrast, Case 2 maintains elevated gradient levels over an extended period, implying sustained scalar filamentation and a greater interfacial area available for diffusion. After their respective peaks, both cases enter a decay regime governed primarily by molecular diffusion. While the relative decay rates appear similar, Case 2 maintains higher absolute values for longer, suggesting that its flow configuration not only generates stronger gradients but also prolongs their presence. This prolonged residence of fine-scale structures enhances the diffusive potential and contributes to the more rapid and complete homogenization observed in scalar variance analysis.

These observations suggest that Case 2's advantage lies primarily in its ability to rapidly amplify gradients after the structural transition at 20 s, thereby increasing the scalar dissipation capacity of the system. In contrast, the prolonged plateau in Case 1 indicates that the flow does not reach the same level of scalar deformation, likely due to the persistence of large-scale coherent flow structures that trap and recirculate fluid elements without promoting filamentation. However, it is important to emphasize that the presence of a plateau in Case 1 does not, by itself, confirm the presence of long-lived unmixed pockets. Rather, it points to a reduced ability to stretch and fold scalar interfaces, which can slow down the homogenization process. Longer simulation times would be required to determine whether Case 1 ultimately reaches a steady asymptote in $||\nabla\varphi||_{L^2}$ or if the scalar gradients continue to decay slowly over time.

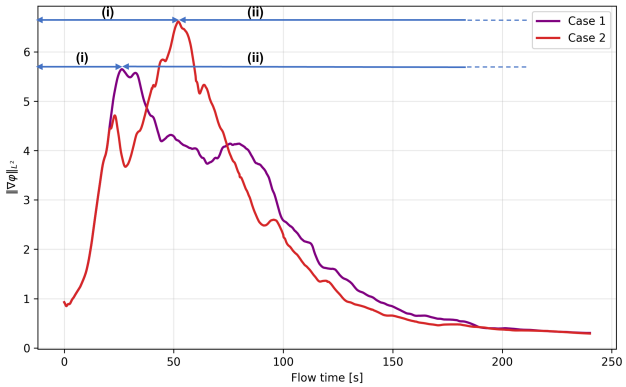

Figure 12: Temporal evolution of the concentration gradient norm $||\nabla\varphi||_{L^2}$ for Case Study 1 and Case Study 2, highlighting (i) the gradient generation phase, associated with interface stretching and scalar filamentation, and (ii) the gradient dissipation phase, dominated by diffusive smoothing and homogenization

Moreover, the gradient dynamics are closely tied to the variance evolution discussed previously (Figure 11). The period in which $||\nabla\varphi||_{L^2}$ remains elevated coincides with the non-exponential variance decay regime, where advective processes dominate over diffusion. For Case 2, this regime is shorter (approximately 0–60 s), whereas in Case 1 it persists until around 80 s. This suggests that the transition from advection-dominated to diffusion-dominated dynamics occurs earlier in Case 2, further reinforcing the idea that the improved jet configuration promotes faster breakdown of large-scale scalar features. Additionally, small oscillations observed in Case 1's $||\nabla\varphi||_{L^2}$ curve during the decay phase could reflect intermittent regeneration of scalar gradients through recirculating zones or localized eddies. Such behavior is often associated with flows exhibiting low spatial uniformity of stirring, where scalar stretching is not sustained across the entire domain. In contrast, Case 2 shows a smoother decline, consistent with a more uniform stirring pattern and the progressive elimination of scalar gradients.

3.2.3 Mix norm

The mix norm $\|\varphi\|_m$ serves as a powerful indicator of mixing efficiency due to its spectral sensitivity—it accounts not just for the global scalar magnitude (as with variance), or local gradients (as with $||\nabla\varphi||^2_{L^2}$), but for the redistribution of scalar variance across spatial frequencies. Both Case 1 and Case 2 exhibit a monotonic decline in $\|\varphi\|_m$ throughout the time evolution (Figure 13), consistent with the irreversible tendency of mixing systems toward homogenization. However, Case 2 consistently maintains a lower mix norm, indicating more efficient suppression of intermediate-scale scalar fluctuations.

Early-time regime (20–60 s) reveals marked differences between the two configurations. Case 2 exhibits a significantly steeper initial decline in $\|\varphi\|_m$, pointing to more vigorous stirring or scalar folding mechanisms. This rapid reduction suggests a flow field dominated by transient vortical structures and elevated chaoticity, which accelerate the breakup and redistribution of scalar features. In contrast, the slower decline in Case 1 indicates a more orderly or laminar regime with reduced stirring capacity and delayed filamen-

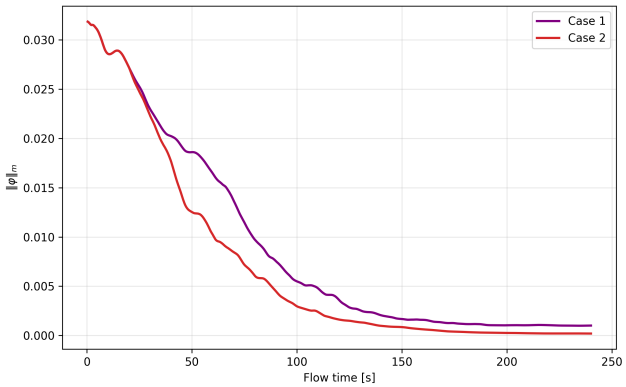

Figure 13: Mix norm $\|\varphi\|_m$ evolution for Case study 1 and Case study 2

tation. As mixing progresses (60–150 s), the decay rate of the mix norm slows in both cases, signaling a partial depletion of easily stretched scalar structures. Nevertheless, the gap between the curves remains clearly pronounced—Case 2 continues to outperform Case 1. This sustained advantage implies that advective mechanisms, although weakening, are still active in Case 2, supporting continuous filamentation and redistribution of scalar content. The reduced mixing efficiency in Case 1 may be due to the emergence of large-scale recirculation zones, which can trap scalar structures and limit interaction across regions. During the final phase (150–240 s), both systems approach a plateau in $\|\varphi\|_m$, indicating that mixing is entering its asymptotic, diffusion-dominated stage. Importantly, Case 2 maintains a lower residual mix norm, suggesting it not only mixes faster but achieves a more complete homogenization.

Over longer timescales, both cases transition into a slower regime dominated by diffusion. Yet even in this asymptotic stage, the persistent gap between the two curves indicates that Case 2 not only initiates mixing more efficiently but also sustains a higher homogenization rate. This advantage may stem from the sustained unsteadiness or time-dependent nature of forcing (e.g., oscillating jets), which continually perturbs the scalar field and inhibits the formation of quasi-steady recirculation zones known to limit mixing.

Crucially, the mix-norm distinguishes between qualitative differences in mixing topologies that variance-based metrics might conflate. Variance-based metrics primarily focus on the overall distribution of concentration values, but they fail to capture the finer spatial details of how the concentration field is distributed across the domain. This means that two scalar fields with identical variance can exhibit very different spatial textures. For instance, one field may have large, coherent regions or "blobs" of similar concentration, which although they result in low variance, indicate poor mixing due to the persistence of large-scale coherent structures. In contrast, a second field might exhibit fine, interspersed filaments of varying concentration values, suggesting a high degree of local variation and more thorough mixing. Despite having the same variance, the latter scenario reflects a much more efficient and advanced mixing state.

The mix-norm captures the variations between neighboring points, with well-mixed fields displaying larger gradients due to their finer-scale distribution, while fields with large, unbroken regions show smaller gradients and thus a higher mix-norm. This sensitivity allows the mix-norm to distinguish between mixing

topologies that may appear similar in terms of variance but differ in their actual degree of mixing, making it a more stringent and precise indicator of mixing quality, rather than just its extent. Importantly, as established in Eq.(47), the mix norm $\|\varphi\|_m$ is mathematically constrained to decay at least as fast as the concentration variance σ_φ^2 in diffusion-dominated systems (Mathew et al., 2005; Thiffeault, 2012). This relationship is borne out in our simulations: both metrics exhibit similar monotonic decay trends, with sharp early-time declines and asymptotic plateaus beyond $t \approx 150$s (Figures 11 and 13).

3.2.4 Effect of Switching Interval

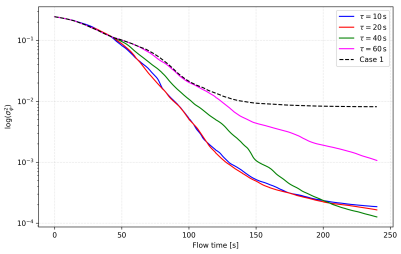

(a) Scalar variance σ_φ^2 on a semi-logarithmic scale

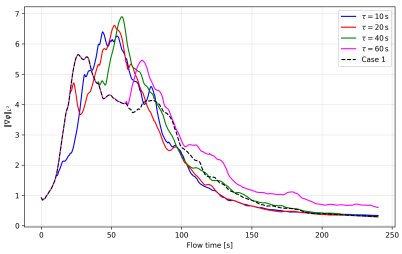

(b) Concentration gradient norm $||\nabla\varphi||_{L^2}$

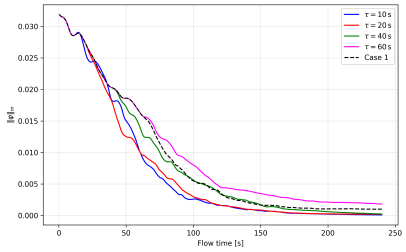

(c) Mixing norm $|\varphi|_m$. Curves for $\tau = 40$ s and $\tau = 60$ s are superposed

Figure 14: Temporal evolution of mixing metrics under different switching intervals ($\tau = 10$, 20, 40, and 60 s) compared with Case I (no switching) for Case Study 2.

Having established that alternating inlet–outlet configurations improve scalar homogenization compared to a fixed setup, we further examined the influence of the switching time τ on mixing performance. The objective was to determine the optimal switching frequency that maximizes homogenization efficiency while remaining consistent with the natural advective timescales of the flow. To this end, we performed simulations for $\tau = 10, 20, 40$, and 60 s. Mixing performance was evaluated using the scalar field metrics introduced earlier (Figure 14). The results reveal a clear hierarchy in mixing performance, with $\tau = 10$ s and $\tau = 20$ s demonstrating nearly identical and superior behavior across all metrics. Both configurations exhibit rapid exponential decay of scalar variance, achieving reduction by three orders of magnitude within approximately 150 seconds. The concentration gradient norm shows similar trends, with both short switching intervals

reaching comparable final values significantly lower than the longer intervals. The mix norm evolution further confirms this equivalence, with $\tau = 10$ s and $\tau = 20$ s following nearly overlapping trajectories and achieving the most effective scalar redistribution. In contrast, $\tau = 40$ s demonstrates markedly inferior performance across all indicators. While it initially follows a similar trajectory to the shorter intervals, the decay rates become substantially slower after approximately 100 seconds. The scalar variance plateaus at higher values, and the concentration gradient norm remains elevated, indicating incomplete mixing and persistent unmixed regions. This degradation suggests that the 40-second interval allows flow structures to develop excessive coherence between switches, reducing the effectiveness of scalar filament stretching and deformation.

The $\tau = 60$ s configuration exhibits the poorest mixing performance by a significant margin. All metrics show dramatically slower decay rates, with scalar variance remaining approximately one order of magnitude higher than the optimal cases throughout the simulation period. The concentration gradient norm displays the most pronounced difference, maintaining values 2-3 times higher than the shorter switching intervals. The mix norm evolution confirms this trend, showing the slowest approach to homogenization. These results indicate that 60-second switching intervals permit excessive stabilization of flow structures, severely limiting the chaotic advection mechanisms essential for effective scalar mixing. As τ increases, the temporal evolution of all mixing indicators progressively approaches the behaviour of the fixed-inlet case. In particular, for $\tau = 60$ s the decay rates of scalar variance, gradient norm, and mix norm become nearly indistinguishable from Case 1, indicating that the system effectively reaches the $\tau \to \infty$ limit. This confirms that flow structures at large switching intervals become long-lived and coherent, suppressing the stretching mechanisms responsible for enhanced mixing, and therefore reproducing the performance of the non-switching configuration.

Notably, the convergence of performance between $\tau = 10$ s and $\tau = 20$ s suggests the existence of an optimal switching frequency regime rather than a single critical value. Both intervals appear to capture the essential physics of flow redirection while maintaining sufficient disruption of coherent structures. The scalar mass conservation remains excellent across all cases, as evidenced by the stable spatial average concentration values.

Complementary scalar concentration maps at $t = 80$ s and $t = 120$ s (Figure 15) support these findings. The $\tau = 10$ s case displays rapid filament breakup and large-scale scalar redistribution, while $\tau = 20$ s demonstrates improved coverage compared to $\tau = 40$ and 60 s, with fewer unmixed regions and earlier onset of filament destabilization.

Although $\tau = 10$ s does not strictly align with the advective timescale, its superior homogenization performance makes it the optimal switching time from a purely performance-driven perspective. The slight deviation from the ideal physical timescale does not hinder effective flow development nor compromise scalar conservation. On the other hand, $\tau = 20$ s represents a well-justified compromise. It closely matches the advective time required for scalar–flow interaction to develop meaningfully before redirection. This interval ensures physical coherence in flow evolution while maintaining strong mixing performance, making it particularly suitable in contexts where operational stability, energy efficiency, or shear sensitivity (e.g., in microalgae cultivation) is a concern.

Based on these findings, both $\tau = 10$ s and $\tau = 20$ s represent optimal switching intervals from a mixing efficiency perspective. However, $\tau = 20$ s emerges as the most practical choice for several reasons. First, it achieves mixing performance virtually indistinguishable from the 10-second interval while requiring 50% fewer switching operations, thereby reducing mechanical stress on valving systems and improving operational reliability. Second, the 20-second interval aligns more closely with the natural advective timescales of the system, ensuring that flow structures have sufficient time to develop meaningful momentum before redirection occurs. This physical coherence is particularly important for maintaining energy efficiency and minimizing flow disturbances that could be detrimental to sensitive biological cultures.

The substantial performance degradation observed for $\tau = 40$ s and $\tau = 60$ s establishes a clear lower bound

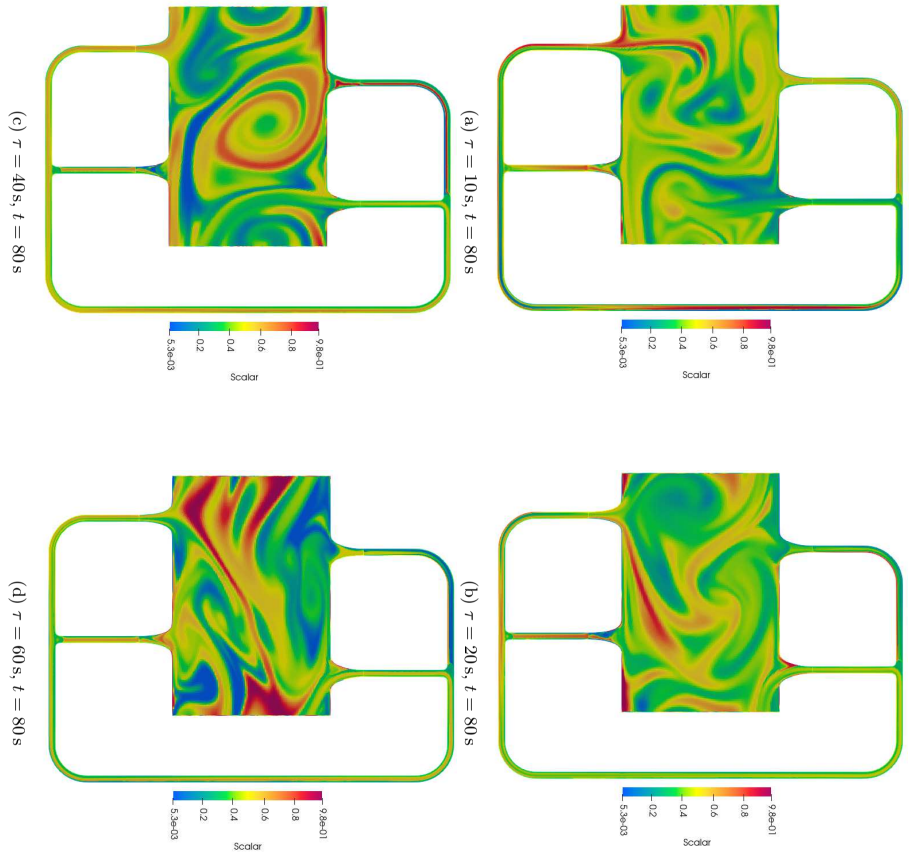

(a) $\tau = 10\,\mathrm{s},\ t = 80\,\mathrm{s}$ (b) $\tau = 20\,\mathrm{s},\ t = 80\,\mathrm{s}$

(c) $\tau = 40\,\mathrm{s},\ t = 80\,\mathrm{s}$ (d) $\tau = 60\,\mathrm{s},\ t = 80\,\mathrm{s}$

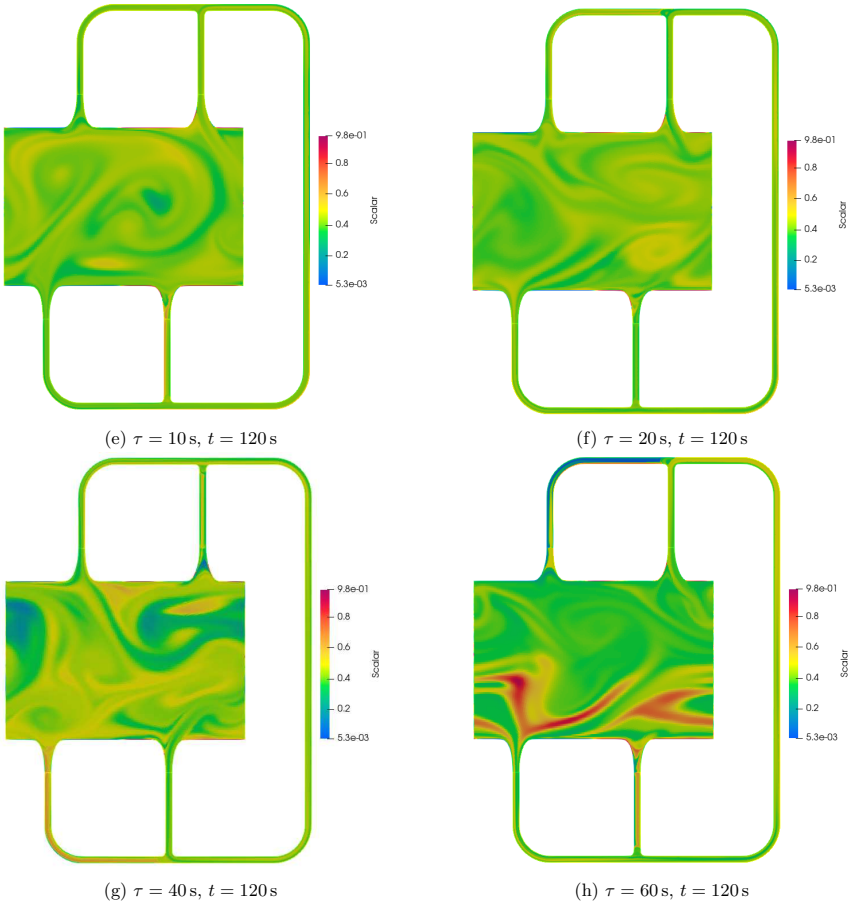

(e) $\tau = 10\,\mathrm{s}$, $t = 120\,\mathrm{s}$ (f) $\tau = 20\,\mathrm{s}$, $t = 120\,\mathrm{s}$

(g) $\tau = 40\,\mathrm{s}$, $t = 120\,\mathrm{s}$ (h) $\tau = 60\,\mathrm{s}$, $t = 120\,\mathrm{s}$

Figure 15: Comparative scalar concentration fields at $t = 80\,\mathrm{s}$ and $t = 120\,\mathrm{s}$ for different switching intervals ($\tau = 10, 20, 40, 60\,\mathrm{s}$) for case study 2

for effective switching frequencies. These longer intervals fail to maintain the dynamic flow asymmetries necessary for chaotic advection, allowing symmetric, stable circulation patterns to dominate and severely limiting scalar transport across the domain.

If the primary goal is to maximize mixing efficiency, then $\tau = 10$ s is the optimal choice. It offers: (i) the steepest decay in scalar variance and concentration norm; (ii) rapid filament stretching and redistribution; and (iii) acceptable mass conservation without significant drawbacks. However, for scenarios involving mechanical limitations or bio-sensitive suspensions, $\tau = 20$ s provides a physically robust and energetically conservative alternative, with minimal compromise in mixing quality. Switching intervals of $\tau = 40$ and 60 s, by contrast, fail to sustain effective mixing and should be avoided in practice.

4 Conclusion

This study evaluated the mixing performance of a novel raceway pond configuration driven by lateral oscillating jets. Two flow strategies were compared: a fixed jet configuration (Case 1) and an alternating jet switching strategy (Case 2). To assess scalar homogenization, we employed several complementary indicators, including the scalar variance, the concentration gradient norm, and the mix-norm—each capturing distinct aspects of the mixing process, from large-scale concentration differences to the dissipation of fine-scale structures.

Case 2 consistently outperformed Case 1 across all metrics. The mix-norm exhibited faster and more sustained decay under the alternating jet strategy, indicating efficient scalar redistribution across scales. The gradient norm revealed a sharp increase followed by rapid decay after the 20-second mark—coinciding with the onset of jet switching—signaling enhanced filament stretching and interface destabilization that promote diffusive mixing. In contrast, Case 1 plateaued early, with persistent large-scale structures and weaker interface dynamics, ultimately hindering further homogenization.

These results demonstrate that lateral jet switching significantly improves mixing by introducing time-dependent shear and disrupting coherent vortical structures. This temporal modulation enhances scalar transport, particularly in regions where geometric constraints would otherwise trap unmixed fluid. The combined use of the mix-norm and gradient norm proved especially effective in capturing both the spatial extent and temporal progression of mixing.

Beyond the comparison of flow strategies, we investigated the effect of switching interval τ on mixing efficiency. Four values were tested: 10, 20, 40, and 60 seconds. Frequent switching ($\tau = 10$ s) produced the fastest decay in all scalar metrics, continuously perturbing flow development and maximizing homogenization. Longer intervals, particularly $\tau = 60$ s, allowed the formation of quasi-steady flow structures that limited filament breakup and scalar dispersion. The $\tau = 20$ s case offered a balanced compromise, aligning well with the advective timescale and preserving strong mixing performance while avoiding excessive mechanical agitation.

Although this study focused on passive scalar transport in a two-dimensional Newtonian setting, the insights extend to the design of hydrodynamic systems for microalgae cultivation. The enhanced mixing observed with the alternating jet strategy has operational benefits: faster homogenization reduces stagnation zones, improves nutrient and light distribution, and lowers the risk of localized biomass settling or nutrient starvation, ultimately supporting higher throughput and more consistent biomass quality. From an energy and economic perspective, conventional paddle-wheel driven raceway ponds typically consume tens to hundreds of watts for small-scale systems, scaling up to kilowatts for larger ponds. In contrast, the alternating jet configuration continuously operates a single pump while modulating flow through valves, reducing active power usage by a factor of approximately 2–4. This lowers operational electricity costs, reduces mechanical wear, and minimizes maintenance demands, while maintaining adequate mixing. Such

a strategy provides a practical route to improve process efficiency in larger-scale operations, where mixing power can be a substantial fraction of operating expenses.

Overall, the methodological framework established here provides a robust basis for evaluating and optimizing time-modulated flow strategies in raceway ponds and other open-channel bioreactor systems. By combining improved mixing performance with potential operational and economic advantages, the alternating jet approach offers a promising pathway for enhancing energy efficiency, productivity, and resilience in microalgal cultivation. Future work should consider three-dimensional effects, the rheology of non-Newtonian suspensions, and the coupling between hydrodynamics and biological growth.

Declarations

Author contributions: CRediT

Imane Skifa : Conceptualization, Methodology, Investigation, Validation, Writing - Original Draft, Writing - Review & Editing. **Andrés Cimino** : Conceptualization, Methodology, Investigation, Validation, Review & Editing. **Pierre-Henri Cocquet**: Supervision, Validation, Writing - Review & Editing, Project administration, Funding acquisition. **Nicolas Chauchat**: Supervision, Validation, Writing - Review & Editing. **Yves Le Guer**: Supervision, Validation, Writing - Review & Editing, Project administration, Funding acquisition

Funding

The MOMIPOP project received funding from both Région Nouvelle-Aquitaine and the French Ministry of Higher Education and Research (Ministère de l'Enseignement Supérieur et de la Recherche), France. The project is associated with the convention number MOMiPOP: AAPR2022-2022-17538910.

A Appendix A

A.1 Mesh characteristics and quality assessment

Table A.1: Mesh statistics of the computational domain used in simulations.

Element Type	Cells	Faces	Nodes
Hybrid (Quad/Tri)	45,601	93,588	48,063

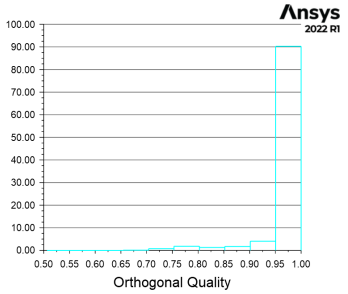

Figure A.1: Distribution of the orthogonal mesh quality. Values close to 1 indicate good orthogonality, ensuring numerical accuracy and stability.

The computational domain was discretized using a hybrid mesh composed of both quadrilateral and triangular elements to accurately conform to the complex geometry of the raceway pond. As summarized in Table A.1, the mesh consists of 45,601 cells, 93,588 faces, and 48,063 nodes. Mesh quality is a critical factor for the accuracy and convergence of CFD simulations, particularly in scalar transport problems involving steep gradients and interface dynamics.

To assess the mesh quality, we evaluated the orthogonal quality distribution across the domain, as shown in Figure A.1. This metric quantifies the alignment between face normals and vectors connecting cell centroids. Values close to 1 denote highly orthogonal cells, which are essential for minimizing discretization errors and ensuring numerical stability, especially in finite volume solvers like those used in ANSYS Fluent. The majority of cells exhibit an orthogonal quality above 0.9, indicating that the mesh is well-suited for resolving both the bulk flow and fine-scale mixing features without introducing significant numerical diffusion. This high-quality mesh provides a robust foundation for the simulation of scalar transport and flow dynamics in the pond.

A.2 Momentum source terms

To accurately model the influence of the pumping system on the flow dynamics, momentum source terms were introduced into the Navier–Stokes equations as volumetric body forces. These source terms represent the pressure increase provided by the pumps and account for pressure losses along the flow paths, including contributions from straight segments, bends, and tees. Table A.2 summarizes the 12 possible configurations tested in this study, each defined by a specific inlet–outlet pair, flow direction, and pump selection. The geometric characteristics of each loop, such as the length (L), number of bends, and tees, were used to estimate minor and major head losses.

The second part of the table details the breakdown of pressure losses for each configuration. Minor losses were calculated based on empirical coefficients for fittings, while turbulent and straight losses were computed

from the Darcy–Weisbach equation, using flow-dependent friction factors. The net pressure gain provided by the pump in each loop, Δp, was derived from the manufacturer's pump curve under nominal flow conditions. These values were combined to obtain the net pressure difference across the loop, which was then converted into a volumetric source term expressed in $\mathrm{N/m^3}$. Positive and negative values of the source term reflect the direction of momentum injection relative to the coordinate system, ensuring consistency with the solver's implementation of directional body forces.

Table A.2: Momentum source terms for 12 possible configurations, defined by different inlet–outlet pairs, flow directions, and pump selections. X and Y refers to the x and y-directions

Loop n	**Inlet**	**Outlet**	**Pump n**	**Dir.**	**L [m]**	**Bends**	**Tees**
1	ES1	ES2	0	X=1	0.399	1	1
2	ES1	ES3	0	X=1	1.33	3	1
3	ES1	ES4	0	X=1	1.429	4	0
4	ES2	ES1	0	X=-1	0.399	1	1
5	ES2	ES3	1	Y=-1	1.231	2	2
6	ES2	ES4	1	Y=-1	1.33	3	1
7	ES3	ES1	0	X=-1	1.33	3	1
8	ES3	ES2	1	Y=1	1.231	2	2
9	ES3	ES4	2	X=-1	0.399	1	1
10	ES4	ES1	0	X=-1	1.429	4	0
11	ES4	ES2	2	X=1	1.33	3	1
12	ES4	ES3	2	X=1	0.399	1	1

Loop n	**Minor Losses [Pa $\times 10^{-3}$]**	**Turb Losses [Pa $\times 10^{-3}$]**	**Straight Losses [Pa $\times 10^{-2}$]**	**Pump Δp [Pa $\times 10^{2}$]**	$S_{momentum}$ **[N/m^3]**
1	1.54	1.89	4.07	5.85	$S_x = 1.95 \times 10^3$
2	4.62	4.97	1.36	1.82	$S_x = 6.06 \times 10^3$
3	6.15	6.15	1.46	2.03	$S_x = 6.77 \times 10^3$
4	1.54	1.89	4.07	5.85	$S_x = -1.95 \times 10^3$
5	3.08	3.79	1.25	1.60	$S_y = -5.34 \times 10^3$
6	4.62	4.97	1.36	1.82	$S_y = -6.06 \times 10^3$
7	4.62	4.97	1.36	1.82	$S_x = -6.06 \times 10^3$
8	3.08	3.79	1.25	1.60	$S_y = 5.34 \times 10^3$
9	1.54	1.89	4.07	5.85	$S_x = -1.95 \times 10^3$
10	6.15	6.15	1.46	2.03	$S_x = -6.77 \times 10^3$
11	4.62	4.97	1.36	1.82	$S_x = 6.06 \times 10^3$
12	1.54	1.89	4.07	5.85	$S_x = 1.95 \times 10^3$

A.3 Pump model validation

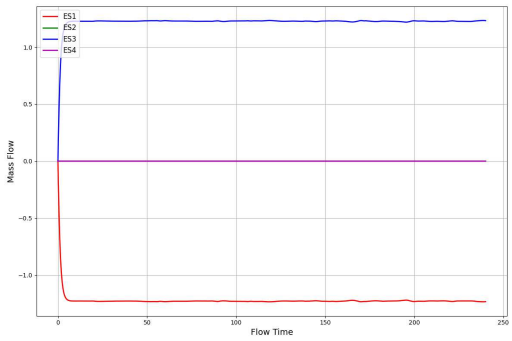

Figure A.2: Time evolution of the mass flow rate at the extraction and supply sections for Case 1 (unidirectional flow from ES3 → ES1)

To validate the implementation of the pump model and ensure physical consistency in the flow boundary conditions, we examined the temporal evolution of the mass flow rate at the inlet and outlet sections for both operating modes. Figure A.2 shows the mass flow rate in Case 1, where a steady flow is imposed from ES1 to ES3. After a brief initialization phase, the mass flow stabilizes quickly and remains constant throughout the simulation, confirming the expected steady-state behavior and the proper enforcement of boundary conditions in the fixed flow configuration.

Case 2, shown in Figure A.3, involves time-dependent switching between two opposing flow directions. At each half-cycle, the active inlet–outlet pair alternates: ES1 → ES3 during the first half, and ES4 → ES2 in the second.

Importantly, across all tested switching intervals (τ = 10, 20, 40, and 60 s), the flow rate consistently stabilizes at the prescribed value well before the onset of the next switching event. This is evident in the nearly symmetric and periodic nature of the mass flow profiles in each case. Even in the shortest interval ($\tau = 10$
texts), the stabilization phase is sufficiently fast to reach a quasi-steady regime within each cycle. For longer intervals (τ = 40 and 60 s), the plateau regions become even more pronounced, underscoring the robustness and responsiveness of the pump control logic.

The numerical pump model accurately reproduces the desired alternation patterns and maintains flow fidelity under both steady and oscillatory regimes. Moreover, the ability to reach a stabilized flow regime within each switching interval ensures that mixing dynamics are not compromised by incomplete flow development. This is essential for a reliable interpretation of scalar homogenization results, especially when evaluating the effect of switching frequency on mixing performance.

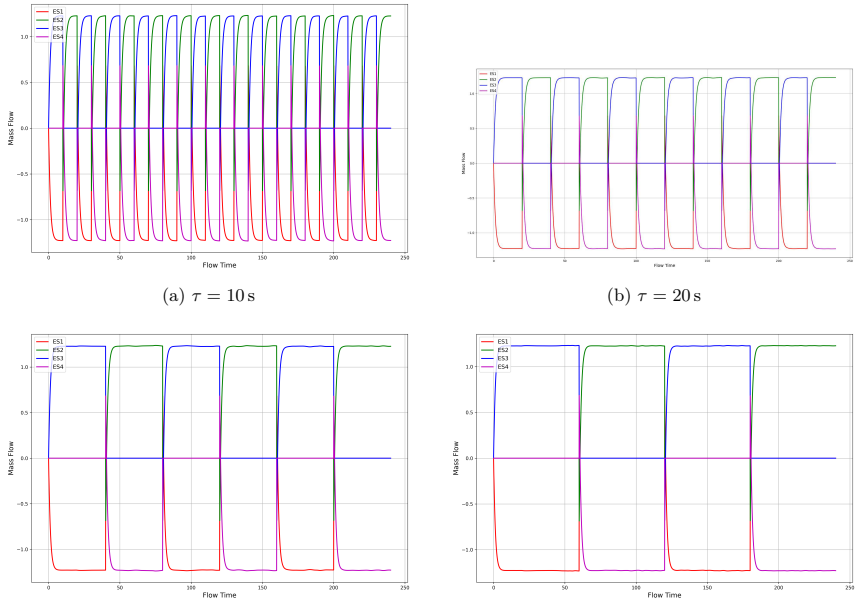

(a) $\tau = 10\,\mathrm{s}$ (b) $\tau = 20\,\mathrm{s}$

(c) $\tau = 40\,\mathrm{s}$ (d) $\tau = 60\,\mathrm{s}$

Figure A.3: Time evolution of mass flow rates at the extraction and supply sections (ES) in Case 2 under different switching intervals: (a) $\tau = 10\,\mathrm{s}$, (b) $\tau = 20\,\mathrm{s}$, (c) $\tau = 40\,\mathrm{s}$, and (d) $\tau = 60\,\mathrm{s}$. Each switching cycle alternates flow direction between ES3 $\rightarrow$ ES1 and ES2 $\rightarrow$ ES4

References

Akca, M. S., Kinaci, O. K., and Inanc, B. (2024). Improving light availability and creating high-frequency light–dark cycles in raceway ponds through vortex-induced vibrations for microalgae cultivation: a fluid dynamic study. *Bioprocess and Biosystems Engineering*, 47(11):1863–1874.

Ali, H., Cheema, T. A., and Park, C. W. (2015). Effect of paddle-wheel pulsating velocity on the hydrodynamic performance of high-rate algal ponds. *Journal of Energy Engineering*, 141(4):04014039.

Andersen, R. A. (2005). *Algal culturing techniques*. Elsevier.

Aref, H. (1987). Stirring by chaotic advection. In *Hamiltonian Dynamical Systems*, pages 725–745. CRC Press.

Aref, H., Blake, J. R., Budišić, M., Cardoso, S. S., Cartwright, J. H., Clercx, H. J., El Omari, K., Feudel, U., Golestanian, R., Gouillart, E., et al. (2017). Frontiers of chaotic advection. *Reviews of Modern Physics*, 89(2):025007.

Batchelor, G. K. (1959). Small-scale variation of convected quantities like temperature in turbulent fluid part 1. general discussion and the case of small conductivity. *Journal of Fluid Mechanics*, 5(1):113–133.

Cant, S. (2001). Sb pope, turbulent flows, cambridge university press, cambridge, uk, 2000, 771 pp. *Combustion and Flame*, 125(4):1361–1362.

Castillo-Sánchez, H. A., de Souza, L. F., and Castelo, A. (2022). Numerical simulation of rheological models for complex fluids using hierarchical grids. *Polymers*, 14(22):4958.

Crank, J. (1979). *The mathematics of diffusion*. Oxford university press.

De Roma, F., Marchisio, D., Boccardo, G., Bouaifi, M., and Buffo, A. (2024). Application of a multiscale approach for modeling the rheology of complex fluids in industrial mixing equipment. *Physics of Fluids*, 36(2).

Dimotakis, P. E. (2005). Turbulent mixing. *Annu. Rev. Fluid Mech.*, 37(1):329–356.

Eltanahy, E., Salim, S., Vadiveloo, A., Verduin, J. J., Pais, B., and Moheimani, N. R. (2018). Comparison between jet and paddlewheel mixing for the cultivation of microalgae in anaerobic digestate of piggery effluent (adpe). *Algal Research*, 35:274–282.

Fox, R., McDonald, A., and Mitchell, J. (2020). *Introduction to Fluid Mechanics*. Wiley.

Gepner, S. and Floryan, J. (2020). Use of surface corrugations for energy-efficient chaotic stirring in low reynolds number flows. *Scientific reports*, 10(1):9865.

Haller, G. (2015a). Lagrangian coherent structures. *Annual review of fluid mechanics*, 47(1):137–162.

Haller, G. (2015b). Lagrangian coherent structures. *Annual review of fluid mechanics*, 47(1):137–162.

Haller, G. and Yuan, G. (2000). Lagrangian coherent structures and mixing in two-dimensional turbulence. *Physica D: Nonlinear Phenomena*, 147(3-4):352–370.

Johnson, D. A., Weissman, J., and Goebel, R. (1988). An outdoor test facility for the large-scale production of microalgae. Technical report, Solar Energy Research Inst., Golden, CO (USA); Microbial Products, Inc., Fairfield, CA (USA).

Kalluri, M. T. and Hillier, A. (2025). Comparing the magnetic rayleigh-taylor instability dynamics in two-and three-dimensions. *arXiv preprint arXiv:2510.27053*.

Karrasch, D. and Keller, J. (2020). A geometric heat-flow theory of lagrangian coherent structures. *Journal of Nonlinear Science*, 30(4):1849–1888.

Kelley, D. H. and Ouellette, N. T. (2011). Separating stretching from folding in fluid mixing. *Nature Physics*, 7(6):477–480.

Kukukova, A., Aubin, J., and Kresta, S. M. (2009). A new definition of mixing and segregation: Three dimensions of a key process variable. *Chemical engineering research and design*, 87(4):633–647.

Li, Y., Zhang, Q., Wang, Z., Wu, X., and Cong, W. (2014). Evaluation of power consumption of paddle wheel in an open raceway pond. *Bioprocess and Biosystems Engineering*, 37(7):1325–1336.

Mathew, G., Mezić, I., and Petzold, L. (2005). A multiscale measure for mixing. *Physica D: Nonlinear Phenomena*, 211(1-2):23–46.

Narala, R. R., Garg, S., Sharma, K. K., Thomas-Hall, S. R., Deme, M., Li, Y., and Schenk, P. M. (2016). Comparison of microalgae cultivation in photobioreactor, open raceway pond, and a two-stage hybrid system. *Frontiers in Energy Research*, 4:29.

Oncel, S. S. (2013). Microalgae for a macroenergy world. *Renewable and Sustainable Energy Reviews*, 26:241–264.

Ottino, J. M. (1989). *The kinematics of mixing: stretching, chaos, and transport*, volume 3. Cambridge University Press.

Rajput, S., Das, B. S., and Sharma, A. K. (2025). Review on modelling approaches of raceway pond: experimental, numerical and machine learning approaches. *ISH Journal of Hydraulic Engineering*, 31(2):382–397.

Rogers, J. N., Rosenberg, J. N., Guzman, B. J., Oh, V. H., Mimbela, L. E., Ghassemi, A., Betenbaugh, M. J., Oyler, G. A., and Donohue, M. D. (2014). A critical analysis of paddlewheel-driven raceway ponds for algal biofuel production at commercial scales. *Algal research*, 4:76–88.

Satyanarayana, K., Mariano, A., and Vargas, J. (2011). A review on microalgae, a versatile source for sustainable energy and materials. *International Journal of energy research*, 35(4):291–311.

Shen, C. (2021). *Investigation of vertical mixing in raceway pond systems using computational fluid dynamics*. Colorado State University.

Shen, C. and Dandy, D. S. (2024). Application of passive vortex generators to enhance vertical mixing in an open raceway pond. *Algal Research*, 79:103434.

Shuba, E. S. and Kifle, D. (2018). Microalgae to biofuels:'promising'alternative and renewable energy, review. *Renewable and sustainable energy reviews*, 81:743–755.

Singla, A., Kumar, N., and Sharma, P. (2010). Biodiesel production from microalgae-a sustainable fuel. *IndianJournals. com*.

Skifa, I., Chauchat, N., Cocquet, P.-H., and Le Guer, Y. (2024). Microalgae cultivation in raceway ponds: Advances, challenges, and hydrodynamic considerations. *EFB Bioeconomy Journal*, page 100073.

Spedding, P., Benard, E., and McNally, G. (2004). Fluid flow through 90 degree bends. *Asia-Pacific Journal of Chemical Engineering*, page 22.

Taylor, G. I. (1953). Dispersion of soluble matter in solvent flowing slowly through a tube. *Proceedings of the Royal Society of London. Series A. Mathematical and Physical Sciences*, 219(1137):186–203.

Thiffeault, J.-L. (2005). Measuring topological chaos. *Physical review letters*, 94(8):084502.

Thiffeault, J.-L. (2012). Using multiscale norms to quantify mixing and transport. *Nonlinearity*, 25(2):R1.

Thiffeault, J.-L. (2021). Nonuniform mixing. *Physical Review Fluids*, 6(9):090501.

Thiffeault, J.-L. (2022). *Braids and dynamics*. Springer.

Thiffeault, J.-L. and Finn, M. D. (2006). Topology, braids and mixing in fluids. *Philosophical Transactions of the Royal Society A: Mathematical, Physical and Engineering Sciences*, 364(1849):3251–3266.

Villermaux, E. (2019). Mixing versus stirring. *Annual Review of Fluid Mechanics*, 51:245–273.

Zhu, S., Lin, Z., Li, L., and Ding, L. (2024). Optimal stirring strategies for passive scalars in a domain with a general shape and no-flux boundary condition. *arXiv preprint arXiv:2401.05684*.